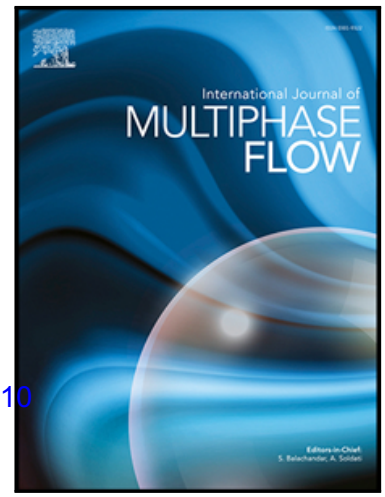


# Bubble column fluid dynamics: novel perspective for flow regimes and comprehensive experimental investigations

Giorgio Besagni

PII: S0301-9322(20)30621-2
DOI: https://doi.org/10.1016/j.ijmultiphaseflow.2020.103510
Reference: IJMF 103510

To appear in: *International Journal of Multiphase Flow*

Received date: 2 January 2020
Revised date: 7 October 2020
Accepted date: 3 November 2020

Please cite this article as: Giorgio Besagni , Bubble column fluid dynamics: novel perspective for flow regimes and comprehensive experimental investigations, *International Journal of Multiphase Flow* (2020), doi: https://doi.org/10.1016/j.ijmultiphaseflow.2020.103510

Highlights

- A comprehensive theory to describe flow regimes in bubble columns is proposed
- A comprehensive experimental investigations are conducted
- Global and local flow properties are experimentally obtained
- Five gas spargers are tested
- The influence of the aspect ratio and liquid phases are discussed

# Bubble column fluid dynamics: novel perspective for flow regimes and comprehensive experimental investigations

Giorgio Besagni[*1]

[1]Politecnico di Milano, Department of Energy, Via Lambruschini 4a, 20156 Milano, Italy

[*] Corresponding author: Giorgio Besagni, giorgio.besagni@polimi.it, Politecnico di Milano, Department of Energy, Via Lambruschini 4a, 20156 Milano, Italy

## Abstract

When a gas phase is injected into a liquid phase, it gives rise to a rich, fascinating and mysterious fluid dynamic phenomenology. The lack of knowledge regarding this phenomenology, a shortcoming in the design and operation of multi-phase reactors, is related to the absence of an unique definition of the flow regimes. To date, different studies gave different definitions of the flow patterns and, subsequently they experimentally obtained some global and local flow properties, with no physical-based description of the flow patterns. Is there a theory able to determine a-priori the boundaries of different flow regimes (and, thus, the flow regime for a given set of boundary conditions, given the phases and the system design)? Answering this question requires changing the present point of view in defining and describing the flow regimes and it is the primary motivation of this paper. To achieve this goal, a new theory has been formulated, which changes the present way of approaching bubble columns and which is based on the following statement: the fluid dynamics in gas-liquid bubble columns is interpreted by means of a general relationship—built upon five flow regime transitions—between two global fluid dynamic parameters. The strategic path to formulate this theory is, first, to go back to the pioneering studies and formulate basic relationships on the basis of a general principle. Subsequently, in order to support and verify the theory a comprehensive and multi-scale experimental investigation has been performed and coupled with previous experimental studies. The different experimental studies have been conducted in a gas-liquid large-scale bubble column (height of 5.3 m; inner diameter of 0.24 m) operated in the batch and in counter-current modes; to study all flow regimes, the bubble column was tested with five gas spargers (viz., pipe sparger in open tube and annular gap configuration, spider sparger, two different perforated plates and needle spargers) with different values of the aspect ratios and different liquid phases. It was found that, in an air-water bubble column, the gas velocity is approximately 0.03 m/s either in the case of the destabilization of the mono-dispersed homogeneous flow regimes or in the case of the destabilization of the pseudo-homogeneous flow regimes. Increasing the gas sparger opening induces a narrowing of the boundaries between the transitional flow regimes; conversely, increasing the bubble column aspect ratio destabilizes the existing flow regimes up to some critical values.

Also, increasing the superficial liquid velocity in the counter-current mode destabilizes the homogeneous flow regime. Finally, it has been observed that the prevailing effect of the liquid phase, in a bubble column operated with a "*coarse*" gas sparger, is to change the boundary of the homogenous flow regime. It has also been discussed how the change in coordinates of the flow regime transition between the homogeneous and the heterogeneous flow regimes is caused by the changes in the size distribution. This study is intended to outline a precise definition of the flow regimes in bubble columns and it poses a rational basis for future studies.

**Keywords.** Bubble column fluid dynamics; Global and local flow properties; Novel theory for flow regimes

# Nomenclature

### Symbols

| | | |
|---|---|---|
| $c$ | Mass or molar concentration | [%] |
| $C_0$ | Distribution coefficient (Eq. (15)) | [-] |
| $C_1$ | Slip velocity (Eq. (15)) | [m/s] |
| $D^*_H$ | Non-dimensional diameter (Eq. (1)) | [-] |
| $d_c$ | Diameter of the column | [m] |
| $D_H$ | Hydraulic diameter (Eq. (1)) | [m] |
| $d_o$ | Gas sparger holes diameter | [mm] |
| $f$ | Relationship between $\varepsilon_G$ and $t_i$ (Eq. (3)) | [-] |
| $G$ | Acceleration due to gravity | [m/s$^2$] |
| $g$ | Relationship between $t_i$ and system parameters (Eq. (4)) | [-] |
| $H_0$ | Height of the free-surface before aeration | [m] |
| $H_c$ | Height of the column | [m] |
| $H_D$ | Height of the free-surface after aeration | [m] |
| $J$ | Drift-flux | [m/s] |
| $n^*$ | Dimensionless concentration | [-] |
| $t_i$ $(i=1,2,3,4,5)$ | Flow regime transition points (Eq. (3)), as displayed in Figure 1 | [-] |
| $U$ | Superficial velocity | [m/s] |
| $u$ | Mean rise velocity of the gas phase | [m/s] |
| $V$ | Volume | [m$^3$] |
| $v$ | Swarm velocity (Eq. (3)) | [m/s] |
| $z$ | Time variable (Eqs. (16)-(17)) | [m/s] |

### Greek Symbols

| | | |
|---|---|---|
| $\mu$ | Viscosity | [N s/m$^2$] |
| $\varepsilon$ | Holdup | [-] |
| $\zeta$ | Relationship between $J_T$ and $z$ (Eq. (16)) | [-] |

| | | |
|---|---|---|
| $\rho$ | Density | [kg/m$^3$] |
| $\chi$ | Relationship between $J_T$ and $z$ (Eq. (17)) | [-] |
| $\Omega$ | Bubble column operating curve (Eq. (3)), relationship between $\varepsilon_G$ and $J_T$ | [-] |

**Subscripts**

| | |
|---|---|
| *b* | Bubble parameter |
| *Cr* | Critical value |
| *G* | Gas phase |
| *L* | Liquid phase |
| *local* | Local gas holdup measurement |
| *T, E* | Subscripts in the drift-flux formulation (Eqs. (5)-(6), (9)-(10)) |
| *trans* | Flow regime transition point |

**Superscripts**

| | |
|---|---|
| ‘ | Change of variables (using $t_1$, coordinates, Eqs. (7)-(8)) |

**Acronyms**

| | |
|---|---|
| *AR* | Aspect ratio ($AR = H_0/d_c$) |
| *BSD* | Bubble size distribution |
| *EtOH* | Ethanol |
| *MEG* | Mono-Ethylene Glycol |
| *NaCl* | Sodium chloride |

**Other**

| | |
|---|---|
| *Batch mode* | $U_L = 0$ |
| *Counter-current mode* | $U_L < 0$ |
| *Co-current mode* | $U_L > 0$ |
| $\langle\text{-}\rangle$ | *Spatial average* |
| $\bar{}$ | *Time average* |

# 1 Introduction

Bubble columns are widely used as contacting devices and multiphase reactors in process and chemical industries; an example of their application is discussed in the review papers of Lima et al. (Lima et al., 2018) and Rollbush et al. (Rollbusch et al., 2015b). Their "*baseline*" layout involves a vessel wherein the gas phase is injected into a stagnant liquid phase in the form of "*dispersed bubbles*" or "*coalescence-induced structures*", as defined in refs. (Besagni et al., 2018b; Montoya et al., 2016). This "*baseline*" layout can be modified by including internal heat exchangers (to control the heat transfer and reaction rates) and a solid-phase (a catalyst), and also by applying co-current/counter-current liquid circulation (to increase the mass transfer rate). Even in the "*baseline*" layout, the coupling between the phases gives rise to rich, fascinating and mysterious fluid dynamics phenomena (Prosperetti, 2004). Since the pioneering work of Shah et al. (Shah et al., 1982), it is recognized that the "*global-scale*" is imposed by the "*local-scale*" and that the coupling between the two scales emerges in the flow patterns (*flow regimes*). The "*bubble-scale*" (i.e., the bubble motion and turbulent eddies that transport the gas phase, as described by ref. (Magnaudet and Eames, 2000)), influences the medium-scale (i.e., turbulent eddies that transport the dispersed phase) and the large-scale (i.e., circulation cells and central plume oscillations) circulation, thereby characterizing the "*reactor*-scale". Mudde (Mudde, 2005) and Risso (Risso, 2018) outlined the past, present and perspective challenges of such multi-scale connections. These two papers have been published ten years apart: although some appreciable advancements have been made, the precise definitions behind multi-scale connections have not been unveiled thus far. Zieghenein et al. (Ziegenhein et al., 2020) stated that the "*bubble-scale*" is determined by the connection of three local parameters (namely, the liquid velocity, void fraction, and bubble sizes); however no analytical model has been proposed thus far. Besagni et al. (Besagni et al., 2017a) suggested that the "*bubble-scale*" determines the "*global-scale*" behavior on the basis of the lift force concept proposed by Lucas et al. (Lucas et al., 2005). More recently, Lucas and Zieghenein (Lucas and Ziegenhein, 2019) experimentally verified that the lift force concept is a determinant in flow regime transitions, supporting our previous speculations. Unfortunately, a precise and analytical description of the connections between the "*local-scale*" parameters as well as their upscaling towards the "*reactor-scale*" in the different flow regimes is elusive to date. For this reason, bubble columns are still modelled using macroscopic methods (i.e., empirical or semi-empirical correlations), rather than physical-based approaches (Besagni et al., 2018b); this is a major shortcoming as empirical/semi-empirical correlations can hardly be applied beyond the range of operating conditions and system designs over which they were obtained. The common approach is to separately study the different scales in terms of

the fluid dynamics parameters (i.e., local void fraction, global void fraction, liquid velocity, bubble size, etc) and subsequently consider the flow regimes as an outcome of the operating conditions, with no precise interpretation of the underlying physics and no general relationship between the flow regimes and flow properties.

Many researchers from different countries have proposed different methods to detect the flow regimes on the basis of qualitative/quantitative approaches. The very first studies regarding bubble column flow regimes[1] were proposed, in the early 70s, by Anderson and Quinn (Anderson and Quinn, 1970) and by Dekwer et al (Deckwer et al., 1973). Later, in the 80s, Shah et al. (Shah et al., 1982) and Maruyama et al. (Maruyama et al., 1981) conducted pioneering studies on bubble columns and mentioned the multi-scale concept underlying the prevailing fluid dynamic phenomena. In the following decades, the number of papers published increased, as reviewed by Shaikh and Al-Dahhan (Shaikh and Al-Dahhan Muthanna, 2007); the plethora of published papers can be also appreciated in the introduction of the study of Besagni et al. (Besagni et al., 2017a), who pointed out the lack of shared definition of the homogenous flow regime. Among the various studies conducted, some notable studies are those conducted by (i) Ruzicka et al. (see, for example, refs. (Ruzicka et al., 2001b; Zahradník et al., 1997)), who studied the duality of the flow regimes in bubble columns, (ii) Nedeltchev et al (Nedeltchev, 2015, 2020), who formalized the maldistribution flow regime, (iii) Montoya et al. (Montoya et al., 2016) and Lin et al. (Lin et al., 1996) who focused on the churn-turbulent flow regime, (iv) Besagni and Inzoli (Besagni et al., 2019; Besagni et al., 2017b), who focused on the mono/poly-dispersed homogeneous flow regime, (v) Lucas and Zieghenein (Lucas et al., 2005; Lucas and Ziegenhein, 2019; Ziegenhein and Lucas, 2019), who focused on lift-force-based stability criteria and (iv) Joshi and co-authors (Bhole and Joshi, 2005; Ghatage et al., 2014; Joshi et al., 2001), who focused on the stability criteria to model the homogeneous destabilization and corresponding flow regime transition. Recently, data analysis methods have been proposed to predict the flow regime and local flow properties (Manjrekar and Dudukovic, 2019); the proposed approaches are interesting from the methodology point of view, but are lacking in terms of fundamental and physically based point of view. Other authors (Monahan et al., 2005), instead, used a computational fluid dynamics approach to predict the flow regime transitions; these approaches are interesting, but are hindered by the lack of knowledge regarding coalescence and break-up closures (Lucas et al., 2020). These issues are far more severe when considering the heterogeneous flow regime, wherein the coupling between the phases presents a real challenge

[1] Also, a broad and vast literature has focused on three phase reactors. This literature is briefly listed in the outlook section, when looking at the perspective of this work.

(Barbosa et al., 2001; Besagni et al., 2018b; Montoya et al., 2016; Shah et al., 1985). This brief literature survey is not exhaustive, but it demonstrates that to date, various studies proposed different definitions of the flow patterns and, subsequently obtained global and local flow properties experimentally, with no physical-based description of the flow patterns.

To summarize, the present gap in knowledge relates to the lack of bottom-up approaches; theoretical studies should define and describe a-priori the flow regimes. Subsequently, experimental studies should provide a comprehensive and multi-scale description of the so-called "*birth and life*" of bubbles under the different flow conditions (Di Marco, 2005). Thus, the lack of knowledge can be summarized by the following question: *is there a theory that can explain all fluid dynamics phenomena in bubble columns, encompassing local and global flow properties?* The answer to this question requires changing the present point of view in terms of defining the flow regimes and it is the primary motivation of this research. To this end, this paper goes back to the pioneering studies of Wallis (Wallis, 1969) and Zuber and Findlay (Zuber and Findlay, 1965) and develops a physical-based multi-scale approach to describe the different flow regimes; subsequently, an experimental study is proposed to clarify, prove and demonstrate the theoretical approach. This study is intended to outline a precise definition of the flow regimes in bubble columns and pose a rational basis for future studies, devoted to modelling the different flow regime transitions and the multi-point flow regime properties.

## 2 Overture: flow regimes in bubble columns

As mentioned earlier, the current approach to studying bubble columns fluid dynamics is chaotic, because of the lack of first-principle methods for flow regime detection and the lack of a unique definition of the flow regimes. For this reason, following Occam's razor principle (Domingos, 1999)[2], the method of approaching bubble column fluid dynamics need to be changed. Hence, a novel theory based on the following statement is proposed: *"the fluid dynamics in gas-liquid bubble columns is interpreted by means of a general relationship—built upon the flow regime transitions—regardless of the system considered".* As this statement is postulated to have general validity, it overcomes the above-mentioned shortcomings.

To turn the statement into a theory, some assumptions should be defined and some basic concepts (i.e., physical-based parameters) should be outlined. Regarding the assumptions, the boundaries of this research are defined on the

[2] Occam's razor principle is translated from Latin into English as "*the simplest solution tends to be the correct one*".

basis of the large-diameter concept, owing to the industrial perspective thereof. The definition of large-diameter bubble columns is related to the fluid dynamics properties and, in particular, to the absence of the slug flow resulting from Rayleigh–Taylor instabilities (Kitscha and Kocamustafaogullari, 1989); interested readers may also refer to ref. (Didwania and Homsy, 1981b). The quantification of these instabilities at the "*reactor-scale*" is obtained by comparing the non-dimensional diameter, $D_H^*$, with a critical diameter, $D_{H,cr}^*$ (Besagni et al., 2017a):

$$D_H^* = \frac{D_H}{\sqrt{\sigma / g\left(\rho_L - \rho_G\right)}} > D_{H,cr}^* \approx 52 \quad (1)$$

In Eq. (1), $D_H$ is the hydraulic diameter of the bubble column, $\sigma$ is the surface tension, $g$ is the acceleration due to gravity, and $\rho_L$ - $\rho_G$ is the density difference between the phases. A bubble column is classified as large-diameter column if $D^*_H$ is greater than $D^*_{H,cr}$ = 52 (Brooks et al., 2012)) (i.e., $d_c \gtrsim 0.13$-0.15 m at ambient conditions, which is also in agreement with the flow map of Shah et al. (Shah et al., 1982)). It should be noted that significant differences are present between large-diameter and small-diameter bubble columns (see ref. (Taitel et al., 1980) for a description regarding small-diameter vertical pipes): accordingly, small-diameter bubble column data cannot be scaled-up to describe large-diameter bubble column fluid dynamics. Regarding the physical-based parameters, we explore the pioneering studies of Wallis and Zuber (Wallis, 1969; Zuber and Findlay, 1965) and we exploit the "*drift-flux*" ($J_T$) concept. $J_T$ is defined as the volumetric flux of either components relative to a surface moving at volumetric average velocity expressed as follows:

$$J_T = U_G\left(1 - \varepsilon_G\right) \pm U_L \varepsilon_G \quad (2)$$

In Eq. (2), $\varepsilon_G$ is the "*gas holdup*" (defined as the volume of the dispersed phase divided by the total volume[3]), $U_G$ is the superficial gas velocity, and $U_L$ is the superficial liquid velocity. The sign on the right-hand side depends on the operation mode of the bubble column: co-current mode (+) or counter-current mode (-); in the batch mode, $U_L$ = 0.

Given the above framework, under the constrains of Eq. (1), we can propose the statement underlying the proposed theory: *"The fluid dynamics of large-diameter bubble columns explicates in six flow regimes and is interpreted by a function of two global fluid dynamics parameters (the drift flux and the gas holdup); the analytical form of the function builds on five flow regime transition points".* The six flow regimes emerging upon increase in the gas flowrate, at fixed

[3] The gas holdup (viz., the global void fraction) determines the mean residence time of the gas phase and, in combination with the size distribution of the dispersed phase, the interfacial area.

system design parameters, phase properties, and operation modes are as follows. First, the "*mono-dispersed homogeneous*" and the "*pseudo-homogeneous*" flow regimes are progressively observed. The former is characterized by a mono-dispersed bubble size distribution, while the latter is characterized by a poly-dispersed one (accordingly with the definition of (Besagni et al., 2018b), based on the lift force underlying physical phenomena (Lucas and Ziegenhein, 2019)). Then, the transition flow regime (named transition flow regime without coalescence-induced structures) begins to be established, by non-stable "*coalescence-induced*" structures, which induce gas holdup oscillations (as discussed by Besagni et al. (Besagni et al., 2019) and which are likely to be related to Ledinegg instabilities[4]). Subsequently, "*coalescence-induced*" structures become stable, thereby characterizing the so-called transition flow regime with coalescence-induced structures. Despite "*coalesce-induced*" structures being present in the bubble column they are not completely developed. Indeed, increasing the gas flow rate resulted in a decrease of the gas holdup, thus unveiling the imbalance between higher gas flow rate and the formation of "*coalescence-induced*" structures, which is a clear indication of a transition process from prevailing fluid dynamics. Finally, stable coalescence-induced structures emerge, and the "*pseudo-heterogeneous*" and the "*pure-heterogeneous*" flow regimes take places. The former is characterized by an equilibrium between increase in the flow rate (in terms of the drift flux) and the formation of "*coalesce-induced*" structures (or cluster of bubbles, when coalescence is inhibited, as discussed by Besagni and Inzoli (Besagni and Inzoli, 2017) and is in agreement with the findings of refs. (Takagi and Matsumoto, 2011; Takagi et al., 2008). This ends in a constant gas holdup for different drift flux values and is an indication that "*coalescence induced*" structures are well established. Conversely, in the "*pure-heterogeneous*" flow regime, increasing the gas flow rate increases the contribution of "*coalescence-induced*" structures. For this reason, in this particular flow regime, the influence of the initial boundary condition is lost. The heterogeneous flow regime, as per the pioneering discussions of Hewitt (Hewitt, 1985), later confirmed by Barbosa et al. (Barbosa et al., 2001) is characterized by large waves transporting the liquid phase. Interested readers may refer to the above-cited papers as well as to the literature survey of Montoya et al. (Montoya et al., 2016).

Following this theory, the bubble column operating curve (viz., the relationships between $\varepsilon_G$ and $J_T$, named $\Omega$) is determined by the above-mentioned five flow regime transition points ($t_i$), though $\varepsilon_G = f(t_i)$:

[4] The Ledinegg instability is representative of the instabilities due to the pressure drop-flow rate. In this case, they are related to the opposite effect induced by the lift force: on one hand, the "*small bubbles*", related to the homogeneous flow regime, spreads in the cross-section of the column and reduce vortices; on the other hand, at higher gas flow rates, the "*large bubbles*" increase up to a critical value, where the first "*coalescence-induced-bubble*" is produced.

$$\varepsilon_G = \Omega(J_T) \rightarrow \varepsilon_G = f(t_i)_{i=1,2,3,4,5} \quad (3)$$

Figure 1 outlines the analytical relationship between the drift flux and the gas holdup (for the sake of clarity, in agreement with Wallis (1969), we present $J_T$ *vs* $\varepsilon_G$, rather than the $\Omega$ function). Each point on the $\Omega$-curve depicts global and local flow properties of the corresponding flow regime. Eq. (3) is based on the five flow regime transition points, which in turn depend on the phase properties, system design (i.e., the bubble column dimensions, gas sparger design, etc) and operation modes, Eq. (4):

$$t_i = g_i(\text{phase properties}, \text{system design}, \text{operation mode}) \quad (4)$$

In summary, changing the system design and/or the phase properties and/or the operation modes induces a variation in the flow regime boundaries and does not influence the flow regime properties themselves, as described by $\Omega$. On the basis of the proposed theory, the bubble column fluid dynamics can be predicted and described a-priori via correct modeling of the flow regime transition coordinates (viz, the gas holdup and drift flux at the flow regime transitions[5]). Once Eq. (4) is known, and given the system design parameters (i.e., the bubble column dimensions, operation mode, distributor design, etc), and the gas and liquid phase properties, the bubble column operation curve can be derived in a straightforward matter using Eq. (3). Thus, a change in the system design and/or in the phase properties induces a change in the boundaries between the flow regimes (Eq. (4)), and does not influence the characteristics of the flow regimes, which are governed by $\Omega$ (Eq. (3)).

Using this perspective, some observed phenomena can be easily explained, i.e., the change in shape of the gas holdup curve upon increasing the gas sparger openings (Sharaf et al., 2016), increasing the liquid phase viscosity (Besagni et al., 2018a), changing the gas phase (Koetsier et al., 1976), and including surfactants (Besagni and Inzoli, 2017). Indeed, in these cases, some of the transition points overlap and/or approach zero; this approach can also explain the outcome displayed in the book of Wallis (1969) (i.e., Figures 9.9, 9.10 and 9.11 in Wallis (1969)). When the previous literature is considered, It is also relevant to consider the experimental activities of Olmos et al. (Olmos et al., 2003), who observed bubble coalescence and coalescence-induced flow structures of the "*pseudo-homogeneous*" flow

[5] The knowledge of these two parameters corresponds to the simultaneous knowledge of the gas holdup and the gas/liquid superficial velocities in the co-current/counter-current mode; conversely, in the batch mode. In the batch mode, it corresponds to the simultaneous knowledge of the gas holdup and the gas superficial velocity.

regimes [6], which is consistent with the present discussion regarding the role of the lift force as a determinant for flow regime transitions. Finally, it has not escaped our knowledge that the shape of the proposed curve in Figure 1 is similar to that proposed by Owen and Hewitt (Owen, 1986) for the pressure gradient distribution (somehow related to the gas holdup in Figure 1) against dimensionless gas velocity (somehow related to the drift-flux in Figure 1) for gas–liquid flow in (small-diameter) vertical pipes (which is provided in appendix A). This observation is interesting and poses the basis for a possible generalization of the proposed theory from a broader perspective. The curve shown in Figure 1 may be a sub-case of a more general operating curve, which also consider the slug-flow regime (whose boundaries disappear for large-diameter systems). Similarly, the outcomes described by of Nedeltchev (Nedeltchev, 2015) are consistent with the present theory. For example, on changing the liquid phase, the author observed changes in the flow regimes and the merging of flow regime transitions; on the basis of the experimental results proposed as follows, the flow regime transition of Nedeltechev between the "*transition*" and the "*churn-turbulent*" flow regimes correspond to the present third flow regime transition points.

On the practical point of view, Figure 1, offers a method to derive the coordinates of the flow regime transition points $t_i$ (viz., $[\varepsilon_{G,trans\text{-}i}, J_{T,trans\text{-}i}]$) by global measurements as follows:

i. First flow regime transition ($t_1$). The proposed theory is an extension of the Wallis (1969) theory as the method proposed by Wallis (1969) can capture only the first flow regime transition. The method is based on the comparison of $J_T$ with a theoretical value of the drift-flux ($J_E$) written in terms of "*bubble swarm velocity*" ($v_b$), whose dependence upon $\varepsilon_G$ varies with the prevailing flow regime:

$$J_E = v_b (1 - \varepsilon_G) \tag{5}$$

The idea is to employ a model for $v_b$ that is valid for the mono-dispersed homogeneous flow regime and plot $J_E$ and $J_T$ in the same graph as a function of $\varepsilon_G$. Since the formulation is valid for the mono-dispersed homogeneous flow regime, it is possible to determine $t_1$ as the point at which the curve of $J_E$ deviates from the curve of $J_T$, (see the green line in Figure 1 – viz., the classical Wallis approach):

$$J_T \neq J_E \tag{6}$$

[6] To reach this conclusion, the bubble column operating curve of Omos et al. (2003), viz., Figure 1 in this manuscript, was drawn.

ii. Second flow regime transition ($t_2$). The author's theory postulated that the poly-dispersed homogeneous flow regime is grounded on the mono-dispersed one. Thus, the Wallis (1969) approach can be applied on the basis of a change in the variables (using $t_1$, coordinates in Eq. (6) as the new origin):

$$\varepsilon_G^{'} = \varepsilon_G - \varepsilon_{G,trans-t_1} \tag{7}$$

$$U_G^{'} = U_G - U_{G,trans-t_1} \tag{8}$$

Consequently, the drift flux written with respect to the new coordinates reads as follows:

$$J_T^{'} = U_G^{'}\left(1-\varepsilon_G^{'}\right) \pm U_L \varepsilon_G^{'} \tag{9}$$

Constructing another theoretical drift-flux function ($J'_E$), the same approach can be applied here (see the blue line in Figure 1), to derive the second flow regime transition:

$$J_T^{'} \neq J_E^{'} \tag{10}$$

iii. Third flow regime transition ($t_3$). The third flow regime transition point is determined on the basis of the maximum value of $J_T$ with respect to $\varepsilon_G$:

$$\varepsilon_{G,trans-t3} = \max(\varepsilon_G(J_T)) \tag{11}$$

iv. Forth flow regime transition ($t_4$). The fourth flow regime transition point is determined on the basis of the constant value of $\varepsilon_G$, at high drift flux values:

$$\frac{\partial \varepsilon_G(J_T)}{\partial J_T} = 0 \tag{12}$$

v. Fifth flow regime transition ($t_5$). The fifth flow regime transition point is determined on the basis of the change of value of $\varepsilon_G$, with respect to the constant value of Eq. (12):

$$\varepsilon_G(J_T) \neq \varepsilon_{G,trans-t_4}(J_{T,trans-t_4}) \tag{13}$$

# 3 Experimental setup and methods

A theory need to be enforced by ad-hoc experimental investigations and, to this end, we designed a comprehensive experimental campaign (encompassing the local and global flow properties) and considering different gas spargers.

## 3.1 The experimental setup and test matrix

The experimental setup is a vertical pipe made of Plexiglas® with $d_c$ = 0.24 m ($D^*_H$ = 88.13, computed as per Eq. (1)) and $H_c$ = 5.3 m, operated in the batch mode at ambient temperature (in the range of 295 ± 1 K, as imposed by the laboratory ventilation and regulation system) and pressure (Figure 2). The pressure of the gas phase is controlled by a pressure reducer upstream from the rotameters (*#1* and *#2* in Figure 2; accuracy ± 2% f.s.v., E5-2600/h manufactured by ASA, Italy). The system temperature has been maintained constant during the tests at room temperature ($T$ = 295 ± 1 K); The value of gas density (used to calculate $U_G$) is computed by using the ideal gas law at the column midpoint conditions (Besagni et al., 2017a; Reilly et al., 1994).

To describe the influence of the boundary conditions on the analytical formulation of Eq. (3), the bubble column has been tested under different values of aspect ratio (as described in the next section) and four different gas spargers have been studied. In particular, three novel gas spargers have been designed and tested besides the data previously obtained for the pipe sparger (open tube and annular gap configurations; gas sparger openings having inner diameter $d_0$ = 3.5, as described in (Besagni and Inzoli, 2016c)) and for the spider sparger (gas sparger openings having inner diameter in the range of $d_0$ = 2.0 – 4.0 mm, located on the side of each arm facing upward as well as in the central cylinder, as described in (Besagni and Inzoli, 2016b)). The three novel gas spargers consist of a sparger zone and a plenum (built in Plexiglas; 0.21 m diameter and 0.21 m height):

1. Needle sparger (see the images in (Besagni et al., 2018a)). The sparger zone consists of plates with 581 holes, with holes having 1.0 mm inner diameter, uniformly distributed about the column cross-section.
2. Perforated plate sparger with $d_o$ = 1.0 mm (see the image in (Besagni et al., 2019)). The sparger zone consists of plates with 581 holes, with holes having $d_0$ = 1.0 mm inner diameter, uniformly distributed about the column cross-section.
3. Perforated plate sparger with $d_o$ = 0.5 mm. The sparger zone consists of plates with 581 holes, with holes having $d_0$ = 0.5 mm inner diameter, uniformly distributed about the column cross-section.

The tested gas spargers are conceived to study the influence of inlet boundary conditions, encompassing both "*fine*" and "*coarse*" gas spargers, as defined by Besagni et al. (Besagni et al., 2019). Filtered and dried air has been used as the gaseous phase and the liquid phase has consisted of deionized water for all the above-mentioned gas spargers. In addition, the spider sparger has been also tested with following liquid phases:

1. the aqueous solutions of sodium chloride (*NaCl*) described in (Besagni et al., 2017a);

2. the aqueous solutions of ethanol (*EtOH*) described in (Besagni and Inzoli, 2017);
3. the aqueous solutions of monoethylene glycol (*MEG*) described in (Besagni et al., 2017b).

## 3.2 The experimental methods

The experimental procedure is structured to identify the flow regimes and, subsequently, to measure the global and the local flow properties in the different flow regimes. The first step is to obtain the *Ω-curve* (viz., Figure 1) by measuring the gas holdup for different superficial gas velocities. To this end, bed expansion technique is applied: it measures the location (height) of the liquid free surface before/after air flows into the column, as in Eq. (14):

$$\varepsilon_G = \frac{V_G}{V_{L+G}} \xrightarrow{\text{Constant cross-section-area}} \frac{(H_D - H_0)}{H_D} \tag{14}$$

In Eq. (14), $V_G$ is the volume of the dispersed phase, $V_{L+G}$ is the total volume, $H_D$ is the height of the free-surface after aeration and $H_0$ is the height of the free-surface before aeration (gas sparger opening is the reference location for height measurements). The uncertainties related to Eq. (14) have been described in the appendix of Besagni et al. (Besagni et al., 2017a), to whom the reader may refer. It is known that the initial liquid level acts as an important boundary condition for the bubble column fluid dynamics (it can be either considered by $H_0$ or the aspect ratio, $AR = H_0/d_c$), as discussed by different authors (Besagni et al., 2017a; Orvalho et al., 2018; Sasaki et al., 2016; Sasaki et al., 2017); to this end, this paper takes this effect into account by varying $H_0$, to ensure $AR$ in the range of $1 \leq AR \leq 15$ for the different gas spargers tested. Once the *Ω-curve* is derived, based on the gas holdup measurements, the boundaries of the different flow regimes can be identified, based on Eqs. (5-13) and, at this point, the corresponding global and local flow properties are studied. First, the gas-holdup curve ($\varepsilon_G$ vs. $U_G$) can be analyzed; second, the local scale is interpreted by optical probe and image analysis measurements, as discussed in the followings. A double-fiber optical probe (manufactured by RBI, France) is inserted into the bulk flow at a distance of $h_{probe}$ = 2.3 m from the bottom of the column ($h$ = 1.9 m from the spider gas sparger and $h$ = 1.8 m for the other gas spargers). As discussed in our previous paper (Besagni and Inzoli, 2016b) as well as by Barrau et al. (Barrau et al., 1999), It is based on the differences between the refractive indexes of the probe tip, gas and liquid phases. The post-processing of its digital signal allows computing the local void fraction $\varepsilon_{G,Local}$ and the bubble velocity $u_b$. The reader may refer to Besagni and Inzoli for a discussion regarding the related uncertainties (Besagni and Inzoli, 2016b); in particular, based on the outcomes of our previous studies, a sampling period equal to $\Delta t_{sampling}$ = 1000 s has been applied. To complete the knowledge regarding the local flow properties, image analysis (general settings f/3.5, 1/1600s, ISO400, resolution 4288 x 2848 pixels) is used

to obtain bubble shape, bubble orientation and bubble size distributions. Images have been acquired at approximately $h$ = 2.4 m from the spider gas sparger and $h$ = 2.3 m from the other gas spargers (500 W halogen lamp). As discussed by Ziegenhein et al. (Ziegenhein et al., 2020), squared boxes filled with water were used to correct the optical distortion of the vertical pipe. For each case, at least 800 bubbles were selected using multiple photos. More information regarding uncertainties of the image analysis are discussed in ref. (Besagni and Inzoli, 2016a, 2019) and, more recently, in ref. (Ziegenhein et al., 2020).

# 4 Results

In the previous sections we proposed a novel perspective to study bubble column fluid dynamics. Thus, for the different cases listed in Section 3.1, the *Ω-curve*s are derived, the flow regimes identified and, subsequently, the prevailing flow properties of the different flow conditions are discussed. It is noted that the theoretical framework discussed in Section 2 can provide a rational basis for all the different *Ω-curve*s presented in the forthcoming sections.

## 4.1 The flow regimes

This section describes the flow regimes, on the basis of the *Ω-curves*. First, the effects of the bubble column design and operation modes are discussed; second, the influence of the liquid phase is elucidated.

### 4.1.1 Influence of the bubble column design and operation mode

This section provides insights into the flow regimes of the bubble column for the different air-water cases studied, based on the *Ω-curve*s displayed in Figure 3 and Figure 4. The former elucidates the effects of the gas sparger design and *AR*, whereas the latter elucidates the effects of the gas sparger and the superficial liquid velocity, in the counter-current mode. In addition, the *Ω-curve*s are post-processed on the basis of the methods described in Section 2 to identify the boundaries of the different flow regimes: as result, the flow regime transitions and the observed flow regimes are summarized in Tables 2 - 8. For the sake of clarity, *Ω-curve*s in Figure 3 and Figure 4 are compared with the gas holdup curves obtained in literature. To this end, the data gathered in ref. (Besagni et al., 2017a) and summarized in Table 1 (refs. (Akita and Yoshida, 1973; Patil et al., 1984; Reilly et al., 1986; Rollbusch et al., 2015a; Ruzicka et al., 2001a; Sasaki et al., 2016; Sasaki et al., 2017; Schumpe and Grund, 1986; Thorat et al., 1998; Wilkinson et al., 1992; Yoshida and Akita, 1965; Zahradník et al., 1997)) have been applied.

An insight into the results is provided, commencing from the perforated plate with $d_0$ = 0.5 mm (Figure 3b and Table 2); the peculiar shape of the *Ω-curve* encompassing all flow regimes (Figure 1) is maintained for all *ARs*. All six flow regimes are observed and the transition superficial gas velocities are approximately constant for *AR* > 2–5. On the contrary, this statement does not apply for the transitional gas holdup, which changes also for higher aspect ratios. On the basis of previous literature, Ruzicka et al. (Ruzicka et al., 2001a) tested a similar gas sparger ($d_o$ = 0.5 mm) and, not surprisingly, obtained *Ω-curves* similar in shape. As for the perforated plate with $d_0$ = 1.0 mm, the situation depicted above is not maintained as, for the highest *AR* tested, the transition flow regimes (both with and without coalescence-induced structures) are not observed (Figure 3c and Table 3). In addition, the transitional gas velocities for the homogeneous flow regime are lower compared with those of the perforated plate with $d_0$ = 0.5 mm. This outcome is somehow expected, as larger gas sparger openings induce a bubble size distribution (*BSD*) shifted towards larger bubbles, which are likely to promote the coalescence phenomena (see also the outcomes in Section 4.2 and previous literature (Ziegenhein and Lucas, 2019)). These observations agree with the outcomes of Thorat et al. (Thorat et al., 1998) and Schumpe and Grund (Schumpe and Grund, 1986) who tested a sieve plate ($d_o$ = 1 mm) and a ring plate ($d_o$ = 1 mm) gas sparger, respectively. It may be concluded that increasing the gas sparger opening induces changes in the *Ω-curves*, via narrowing of the boundaries between the transitional flow regimes. This statement is confirmed by the *Ω-curves* observed for the spider gas sparger (Figure 3d and Table 4); in this case, a peculiar duality of the flow regimes is observed: a homogeneous flow regime and an heterogeneous flow regime, without any transition flow regime in between (viz., some flow regime transitions merge together). This statement is of particular interest: on one hand, it supports the previous discussion by Ruzicka and co-authors (Ruzicka et al., 2001b; Sharaf et al., 2016) regarding the existence of the pure heterogeneous flow regime. On the other hand, it suggests that our previous paper regarding flow regimes in bubble columns with a spider sparger should be re-read from a new and broader perspective. In addition, this outcome suggests that the previous observations of Ruzicka and co-authors (Ruzicka et al., 2001b; Sharaf et al., 2016) are now included within the present approach (Section 2), which is more general It is also noted that above-observed shape of the *Ω-curve* agrees with those obtained in previous literature and, in particular, with those obtained by Sasaki et al. (Sasaki et al., 2016; Sasaki et al., 2017), Patil et al. (Patil et al., 1984), Yoshida and Akita (Yoshida and Akita, 1965), Wilkinson et al. (Wilkinson et al., 1992), who tested the so-called "*coarse*" and "*very-coarse*" gas spargers. A similar shape was obtained by Rollbusch et al. (Rollbusch et al., 2015a), who tested a perforated plate gas sparger ($d_o$ = 1 mm); however they used nitrogen as the gas phase. It is also observed that the transition superficial gas velocities are approximately constant for *AR* > 5, as also observed by

Besagni et al. (Besagni et al., 2017a). At this point of the discussion, one may argue that the gas sparger opening is the prevailing driving force for the bubble column operating curve. This is partially true, as the gas sparger opening should be considered along with the *AR* value. Indeed, when the *Ω-curves* of the needle gas sparger are considered, it is noted that decreasing *AR* leads to the merging of some flow regime transitions and, for aspect ratios above 2, the transition flow regimes are not observed anymore. To understand the differences between the needle sparger and the perforated plate with $d_0$ = 0.5 mm (both classified as "*fine gas sparger*", (Besagni et al., 2018b)), it should be noted that the bubble nucleation phenomena in these cases are different: in the case of needles, the bubble nucleation surface is inclined as the needles employed are biomedical ones. This induces a swirled injection of the bubbles and thereby a more intense recirculation at the gas sparger level. This is a possible cause for the instability of some flow regimes. It is noteworthy that the gas velocity is approximately 0.03 m/s in the case of (i) the destabilization of the mono-dispersed homogeneous flow regimes or (ii) the destabilization of the pseudo-homogeneous flow regimes in bubble column with large gas sparger openings. This outcome is of practical importance and provides a precise view of the aspects that are effectively estimated when using the correlations of Reilly et al. (Reilly et al., 1994) or Ribeiro (Ribeiro, 2008). The above-mentioned value of 0.03 m/s is also in agreement with that reported by Nedeltchev and co-workers (Nedeltchev, 2015). In addition, when the present values are compared with those reported by Nedeltchev (Nedeltchev, 2015), it is noted that the "*transition*" and the "*churn-turbulent*" flow regimes correspond to the present third flow regime transition points. Most importantly, this consideration is consistent with the outcome of the stability analysis detailed by Joshi and co-authors (Joshi et al., 2001) and also applied by other authors in two- and three-phase systems (Besagni and Inzoli, 2016a; Bhole and Joshi, 2005), wherein a single transition point at the end of the homogeneous flow regime is detected. Future studies can review the implementation of the stability analysis, as explored by Besagni and Inzoli (2016a), as the data thereof should be included with details regarding bubble sizes and balance forces in dense bubbly flows.

The data presented in Figures 3–6 confirm that, regardless of the experimental setup, increasing the bubble column *AR* destabilizes the existing flow regimes up to some critical values. These observations provide a broader interpretation of some widely accepted phenomena regarding the critical value of the aspect ratio, for which outcomes exist that are independent of the initial liquid level (Ruzicka et al., 2001b; Sharaf et al., 2016). As far as *AR* is concerned, Sasaki et al. (Sasaki et al., 2016; Sasaki et al., 2017), Ruzicka et al. (Ruzicka et al., 2001a), and Thorat et al. (Thorat et al., 1998) found that an increase in $H_0$ causes a decrease in the gas holdup. Indeed, there are two opposite effects (viz., AR and $d_0$), which act to define the bubble column operating curves. This is also clear when the outcomes

of Patil et al. (Patil et al., 1984) are examined; they observed a very low effect of *AR* on the gas holdup. This behavior can be explained by the "*very-coarse*" gas sparger used. To summarize, we can state that three phenomena tend to destabilize the homogeneous flow regime in short bubble columns, as discussed by Besagni et al. (Besagni et al., 2017a) and Xue et al. (Xue et al., 2008). These are the more relevant coalescence phenomena, non-developed liquid circulations patterns and the higher extent of the end-effects. It should be noted, that for a comprehensive understanding the effect of AR on transitions, BSDs need to be measured with respect to height for all *AR*, which is a matter of future studies (interested readers may refer to Besagni and Inzoli (Besagni and Inzoli, 2019), who proposed a comprehensive dataset of BSDs at different heights, for a fixed *AR*, which should be extended in future studies). On the other hand, larger gas sparger openings, generated at the gas sparger (which have a negative lift coefficient; see refs. (Lucas et al., 2005; Lucas and Ziegenhein, 2019; Ziegenhein and Lucas, 2019) tend to migrate toward the center of the column, thereby promoting the appearance of the "*coalescence-structures*" and, subsequently, the flow regime transition. On the contrary, the small bubbles stabilize the homogeneous flow regime as the positive lift coefficient tends to spread them over the whole cross-section of the bubble column (Mudde et al., 2009). The author's experimental observation agrees with the expectations and clearly shows that the inlet *BSDs* significantly influence the stability of a bubble column. In particular, a stable bubble bed produced by the gas sparger can not only stabilize the homogeneous flow regime (as widely accepted) but also ensure the existence of all the flow regimes, regardless of changes in the end-effects. In summary, our observations generalize the previous findings. When the effects of the superficial liquid velocity in the counter-current mode (Figure 4) are considered, it is observed that the prevailing effect is shifting the *Ω-curves* (thereby causing destabilization of the homogeneous flow regime). Additionally, in some cases, at very high liquid velocities, the pseudo-heterogeneous flow regime appears, as observed for the pipe sparger (open tube configuration, Figure 4a) and spider sparger (Figure 4c). The appearance of additional flow regimes, can be explained by a higher relevance of end-effect; instead, the shifting of the *Ω-curves* can also be explained by the local measurements as per ref. (Ziegenhein et al., 2020), which demonstrate the matter in which the counter-current operation tends to downshift the local liquid velocity profiles. In general, the relevant effect of the liquid flow rate is likely to be related to the comparable order of magnitudes of the liquid and gas velocities (Hills, 1976). The destabilization of the homogeneous flow regime can be explained as the counter-current liquid slows the bubbles (Ziegenhein et al., 2020) and increases the local gas holdup and local void fraction. Hence, for a given superficial gas velocity, the mean distance between the bubbles decreases, and coalescence phenomena may occur more easily. When the annular gap and open tube configurations are compared for the pipe sparger (Besagni and Inzoli, 2016c), it

is noted that the absence of internals destabilize the homogeneous flow regime. Besagni and Inzoli (Besagni and Inzoli, 2016b) explained that this observation might be related to the gas sparger configuration, wherein higher bubble coalescence is caused in the region upstream of the sparger, when no internal is present.

### 4.1.2 **Influence of the liquid phase properties**

The previous section discussed how the boundaries between the flow regimes for a fixed liquid phase are related to the simultaneous contributions of the gas sparger design and *AR*. This section further discusses the influence of the liquid phase. First, the influence of surfactants is discussed, considering both organic (*EtOH*, Figure 7) and inorganic (*NaCl*, Figure 8) active compounds. Subsequently, the influence of a viscous liquid phase (*MEG*, Figure 9) is elucidated. It is worth noting that surfactant-based mixtures and *MEG*-water mixtures at very low *MEG* concentrations are classified as "*non-coalescing*" and in this the "*coalescence-induced*" structures are composed of clusters comprising small bubbles. This phenomenon has been already been described in ref. (Besagni et al., 2016) and does not influence the general framework discussed in Section 2. In Figures 7–9, it can be seen that, starting from the baseline case of a spider sparger bubble column operated with air and water, the prevailing effect of the liquid phase changes the boundary of the homogenous flow regime.

In particular, the effect of organic substances, for different *ARs* and ethanol concentrations (*c*) are shown in Figure 7. As the gas sparger openings are fixed, two concurrent effects are observed: (a) *AR* destabilizes the homogeneous flow regimes and (b) when increasing ethanol concentration, the homogenous flow regime is progressively stabilized owing to the coalescence suppression (organic substances are progressively attracted towards the bubble interface), and at higher concentration a dual effect is observed, as described by Guo et al. (Guo et al., 2017). The latter observation can be explained by the changes in the physical properties of the liquid phase as well as the interfacial changes at the bubble interface. Similar results were also observed in *NaCl*-water mixtures (Figure 8); increasing the *AR* destabilized the homogeneous flow regime and increasing the *NaCl* concentration stabilized the homogeneous flow regime. The experimental observations are presented using the dimensionless concentration, $n^*$, which is defined as the ratio between the molar concentration and a critical molar concentration ($c_t$, which is equal to 0.145 mol/l in the case of NaCl (Zahradník et al., 1999)). Practically, increasing the molar NaCl concentration progressively reduces the coalescence rate, up to the critical concentration. Thus, a "*coalescent*" ($n^* < 1$) and a "*non-coalescent*" liquid phase ($n^* > 1$) can be distinguished. It is worth mentioning that Ribeiro Jr. and Mewes (Ribeiro Jr and Mewes, 2007) stated

that the dimensionless concentration can be a similarity criterion for different electrolytes. Accordingly, the *Ω-curves* in Figure 8 might be interpreted with a broad generality.

Figure 9 shows the *Ω-curves* for the binary MEG-water system, considering both the spider (Figure 9a and Figure 9b) and needle spargers (Figure 9c). In the case of a spider sparger, the "*dual effect of viscosity*" is observed as mentioned in (Besagni et al., 2017b). Starting from the baseline case, first, the homogeneous flow regime is progressively stabilized ("*low viscosities*") and is subsequently destabilized ("*moderate/high viscosities*") without changing the prevailing shape of the *Ω-curves.* This supports the above statement that in a bubble column operated with a "*coarse*" gas sparger, the prevailing effect of the liquid phase changes the boundary of the homogenous flow regime. The change in coordinates of the flow regime transition between the homogeneous and the heterogeneous flow regime is caused by the changes in size distribution and this will be discussed in Section 4.2. In contrast, when changing the liquid phase in a bubble column operated with a "*fine*" gas sparger, the *Ω-curves* progressively change their shape, and merges the flow regime transition points, thereby leading toward the previously discussed duality of the flow regimes.

## 4.2 **Characteristics of the flow regimes**

In this section the global flow (viz., the gas holdup curves) and the local flow (viz., the bubble size, the local gas holdup and the local gas velocity) properties are discussed. The previously obtained gas holdup curves and local flow properties for the pipe sparger (Besagni and Inzoli, 2016c)), spider sparger in the counter current mode (Besagni and Inzoli, 2016c)) that is operated using sodium chloride (Besagni et al., 2017a), aqueous solutions of ethanol (Besagni and Inzoli, 2017)) and aqueous solutions of monoethylene glycol (Besagni et al., 2017b) are not presented here. . For more details please refer to the data and curves presented in the above-mentioned references.

### 4.2.1 **The global flow properties**

This section further describes the previously discussed operating curves, based on the gas holdup curves, which is displayed in Figure 10 (needle sparger), Figure 11 (perforated plate with $d_0$ = 0.5 mm), Figure 12 (perforated plate with $d_0$ = 1.0 mm) and Figure 13 (spider sparger). To support the discussion, as stated above, the influence of the bubble column design, operation mode, and the liquid phase properties have been discussed based on previous experimental studies proposed by the author.

When considering these results, it is worth stating that, applying a simple mass conservation balance to the gas phase, $\varepsilon_G$ might be computed as $U_G/u_G$, where $u_G$ is the mean rise velocity of the gas phase. If the bubbles did not interact with the other bubbles or with the wall boundaries, they traveled at their terminal velocities. In this ideal case, $\varepsilon_G$ will increase linearly with $U_G$. In real cases, the coupling between the phases (viz., the interactions between different bubbles and interactions between the gas phase and the liquid phase: the hindrance effect described by (Ruzicka et al., 2001a; Zahradník et al., 1997)) will cause deviations from the theoretical expectations. Therefore, in the mono-dispersed and in the poly-dispersed homogeneous flow regime, the hindrance effect reduces the bubble velocity, thus increasing $\varepsilon_G$. By contrast, in the transition flow regimes and in the heterogeneous flow regimes the strong coupling between the phases as well the possible presence of "*coalescence-induced*" structures cause $\varepsilon_G$ to decrease less than proportionally to $U_G$. From the experimental results it was found that the data support the discussion proposed in Section 4.1 by demonstrating the underlying meaning of the *Ω-curves*. These data also support the statement that the flow regime transitions determine the prevailing shape of the gas holdup curves. The modifications in the gas holdup curve when changing the aspect ratio of the gas sparger design can be easily explained, based on the location of the flow regime transition, and can also provide a physically based explanation to two rule of thumbs: (a) "*fine gas spargers*" produce mono-dispersed size distributions, leading to the hindrance effect, which is physically manifested by the peak on the *S-shaped* gas holdup curve; and (b) "coarse gas spargers" lead to monotonic increase in gas holdup curves.

Upon comparing the different cases, it was observed that the smaller the value of $d_0$, the higher $\varepsilon_G$. This is because of the existence of the mono-dispersed homogeneous flow regime. This flow regime is characterized by the presence of small bubbles with a positive lift coefficient, which reduce the liquid recirculation and thus, it increase the mean residence time of the gas phase (Besagni et al., 2017b). The relationship between $\varepsilon_G$ and $U_G$ is influenced by the nucleation process as the gas sparger size and gas sparger shape are strongly related to the bubble formation patterns (Gaddis and Vogelpohl, 1986). This suggests that the flow regime transition modeling in Eq. (4) needs to consider the physics of the bubble nucleation to model the entire bubble column operating curve. Finally, in the fully developed heterogeneous flow regime the gas holdup values are quite similar. This conclusion suggests that the influence of the sparger design is lower only in the so-called pure heterogeneous flow regime. An insight is proposed in the following, starting from the perforated plate with $d_0$ = 0.5 mm; in this case, the presence of all the flow regimes described in Section 4.1 manifest in the gas holdup curves that maintain the prevailing reversed *S-shaped* curve for all the aspect ratio. The readers may refer to the study of Molerus and Kurtin (Moleurs and Kurtin, 1985) that proposed the

analytical description of the maximum gas holdup in a "*fine*" sparger bubble column. This observation is explained by the stabilizing effect of the employed gas sparger that produces a uniform bubble bed, which stabilizes all the flow regimes regardless of end-side effects. Therefore, changing the aspect ratio does not affect the existence of the different flow regimes, but rather changes the gas holdup values. In this case, the gas holdup decreases continuously while increasing *AR* till the critical *AR* equals to 12.5. As for the perforated plate with $d_0$ = 1.0 mm, this situation is not maintained as, for the highest aspect ratio tested, the transition flow regimes (with and without coalescence-induced structures) are not observed. The existence or disappearance of the flow regimes physically manifest as a change in the gas holdup curves. At higher *AR*, the gas holdup curves change to monotonically increasing curves. This result also provides an explanation for the findings of Thorat et al. (Thorat et al., 1998), sieve plate gas sparger ($d_o$ = 1 mm), and Schumpe and Grund (Schumpe and Grund, 1986), ring plate gas sparger ($d_o$ = 1 mm). Finally, in the case of the perforated plate with $d_0$ = 1.0 mm, the gas holdup decreases continuously while increasing *AR* till the critical *AR* equal to 10. As mentioned in Section 4.1, increasing the gas sparger opening, changes the boundaries of the flow regimes and progressively moves towards a two-regime. Indeed, in the spider design or in the pipe sparger, a duality of flow regimes is observed and, because of the homogeneous and pure-heterogeneous flow regimes, a monotonic gas holdup curves which is concave in shape takes place. This shape is similar to the one observed in refs. (Sasaki et al., 2016; Sasaki et al., 2017; Wilkinson et al., 1992; Yoshida and Akita, 1965). In the "*pseudo-homogeneous*" flow regime, the relationship between the gas holdup and the superficial gas velocity is linear, followed by a change in slope is caused by the appearance of "*coalescence-induced*" structures, which reduces the mean gas residence time in the bubble column. In this case, the gas holdup decreases continuously while increasing *AR* till the critical aspect ratio equals 5, and this is in agreement with (Wilkinson et al., 1992). Looking at the influence of the operation mode, the duality of the flow regimes is still observed; the prevailing effect of the counter-current mode causes a rapid increase in the gas holdup. This outcome has been observed by Besagni and Inzoli (Besagni and Inzoli, 2016b, c) in the different bubble column design and has been verified by the comparable order of magnitude with the gas velocities. Finally, the needle gas sparger is an intermediate situation is observed as it is neither *S-shaped* or concave, despite the small gas sparger openings. This is cased, by the bubble nucleation at the gas sparger level: the bubble nucleation surface is inclined ,as the needle employed are biomedical needles. This induces a swirled injection of the bubbles and, thus causes a more intense recirculation at the gas sparger level. In the previous section we observed that some flow regimes were not observed for the needle sparger: (i) that is, at the lower *ARs*, the gas holdup curves are monotonically increasing and, subsequently, they slowly decrease; (ii) that is, at the increasing *ARs*, the gas holdup

curves tend to be monotonically increasing and, finally, they are slightly reversed *S-shaped* curves. Finally, in this case, the gas holdup decreases continuously while increasing AR till the critical aspect ratio equals 10. In general, these data also support and clarify the discussion in Section 4.1. In addition, our experimental observations confirm the existence of a critical *AR* above which the gas holdup does not depend on *AR*. The value of the critical *AR*, which is equal to 5 (Wilkinson et al., 1992), is confirmed only for the spider gas sparger. When modifying the boundary conditions (i.e., the gas sparger openings), this value changes, that is, the smaller the $d_o$, the higher the critical *AR*; this is in agreement with the outcomes and the considerations of Besagni et al. (Besagni et al., 2017a), as its value is likely to be influenced by the coalescence phenomena.

The above-mentioned discussion considered the air-water flows and demonstrated the concurrent effect of the gas sparger and AR in determining the overall gas holdup curves. However, as mentioned in Section 4.1.2, a third effect should also be considered, that is, the effect of liquid phase properties. It has been shown in Section 4.2.1 that the prevailing effect of changing the liquid phase properties in "*coarse*" sparger bubble columns changes the boundary of the homogeneous flow regime. Accordingly, the gas holdup curves are modified and a stabilization/destabilization of the homogeneous flow regime induces a faster/slower increase in the gas holdup. In particular, the stabilization of the homogeneous flow regime is because of the presence of clusters of bubbles, whereas the destabilization of the homogenous flow regime is because of the high coalescence rate. This is verified by the experimental observations of Besagni and co-authors. First, Besagni et al. (Besagni and Inzoli, 2017; Besagni et al., 2016) proved that increasing the ethanol concentration (up to a certain value, to avoid foaming phenomena (Besagni and Inzoli, 2017)), increases the gas holdup. Besagni and Inzoli (Besagni and Inzoli, 2015, 2016b) also studied the effect of electrolyte concentration and observed that the gas holdup increases continuously while increasing the electrolyte concentration till it reaches the critical concentration. In addition to the above-mentioned literatures, it is worth mentioning the findings of Koetsier et al. (Koetsier et al., 1976), wherein the effects of electrolyte concentration and phase properties on the gas holdup are discussed. Moreover, such effects can be easily explained by the changes in the flow regime transition points. Finally, water-MEG mixtures showed the so-called "*dual effect of viscosity over the gas holdup*" (Besagni et al., 2017b), which was in agreement with the dual effect of the flow regime transitions, that is, up to $c_{MEG,wt}$ = 5%, the gas holdup continuously increases with the increase in MEG concentration (non-coalescent mixture), and then decreases (highly coalescing mixture populated by creating large cap-bubbles). As stated in Section 4.1.2, when changing the liquid phase in the needle sparger bubble column, the flow regimes change and the flow regime transitions merge.

Accordingly, Besagni and Inzoli (Besagni et al., 2018a) observed a progressive change in the shape of the gas holdup curve from *S-shaped* to a concave shape.

### 4.2.2 The local flow properties

This section further discusses the operating curves, based on the local flow properties. In particular, Figure 14 shows the *BSDs*, for the different gas spargers both near the wall and in the center region. The local gas holdup profiles are displayed in Figure 15a (needle sparger), Figure 16a (perforated plate with $d_0$ = 0.5 mm), and Figure 17a (perforated plate with $d_0$ = 1.0 mm), whereas the local gas velocity profiles obtained by the optical probes are displayed in Figure 15b (needle sparger), Figure 16b (perforated plate with $d_0$ = 0.5 mm), and Figure 17b (perforated plate with $d_0$ = 1.0 mm). The *BSDs* and local flow properties for the pipe sparger (Besagni and Inzoli, 2016c), spider gas sparger (Besagni and Inzoli, 2016b, 2019) in air-water and the spider gas sparger with binary mixutures (Besagni et al., 2017a; Besagni and Inzoli, 2017))(Besagni et al., 2017b) are not discussed here.

In general, it is observed that the needle sparger and the perforated plate with $d_0$ = 0.5 mm, produce *BSDs* mostly below the equivalent diameter for the change of sign of the lift force (refer to Ziegenhein and Lucas (Ziegenhein and Lucas, 2019) for a discussion regarding its precise value). In both the cases, *BSD* is unimodal and it is narrower in the case of the needle sparger, owing to the design of the needle (viz., the bubble nucleation is different from the case of a perforated plate, thus causes smaller bubbles to be produced; for more details refer to ref. (Gaddis and Vogelpohl, 1986)). In contrast, the perforated plate with $d_0$ = 1.0 mm produces broader *BSDs*, owing to the larger gas sparger openings. In all cases, increasing $U_G$, makes the size distribution broader and move it towards larger equivalent diameters, as observed in our previous studies and in Jin et al. (Jin et al., 2013). Similarly, other authors (Kang et al., 2000; Muroyama et al., 2013; Xue et al., 2008) observed that the BSD become broader while increasing $U_G$. The BSDs for the spider gas sparger have been presented and discussed in ref. (Besagni and Inzoli, 2016b, 2019), showing a clear poly-dispersed nature of the homogenous flow regime. Measuring the size distribution and morphology of the gas phase in the heterogeneous flow regime is beyond the scope of this study. The interested reader might refer to Kang et al. (Kang et al., 2000), wherein a unimodal distribution in the homogeneous flow regime, a bimodal distribution in the transition flow regime and a unimodal distribution in the heterogeneous flow regime was observed. In all cases, it was observed that *BSDs* near the wall are slightly smaller than the ones in the central region. This effect is likely caused by the lift force (Lucas and Ziegenhein, 2019), which acts on the *BSDs* imposed by the gas sparger with multi-scale effects. The multi-scale effect induces the migration of the bubbles, thus determining the

existence/disappearance and stabilization/destabilization of the flow regimes (this was also confirmed by Besagni and Inzoli (Besagni and Inzoli, 2016b) by observing the *BSDs* in the counter-current mode). It is well known that the smaller bubbles spread in the cross-section of the column, whereas, the larger bubbles, tend to migrate from the low liquid velocity region towards the high liquid velocity regions (viz., in the batch mode, towards the center of the column). The presence of small bubbles, produced by a "*fine*" gas sparger, ensure the existence of mono-dispersed homogeneous flow regime sub-layer, whereas larger bubbles induce destabilization effects. The above-mentioned discussion only considered the effect of gas sparger design; the other two effects, that is, AR and the liquid phase properties should be considered as well. The former will be discussed in future studies, whereas the latter has been discussed for the "*coarse*" sparger in refs. (Besagni et al., 2017a; Besagni and Inzoli, 2017; Besagni et al., 2017b). In particular, organic and inorganic active compounds reduce the coalescence rate, however they do not affect the break-up rate and, accordingly, they shift the *BSDs* toward lower equivalent diameters, and changes the size distribution from bimodal to unimodal. Such change in the size distribution cannot counter-balance the larger bubbles produced at the gas sparger level and, thus, a mono-dispersed homogeneous flow regime cannot be ensured. Considering the influence of MEG concentration, a "*dual effect of viscosity on the size distribution*" is observed, which provides a "*bubble-scale*" explanation of the dual effect on the flow regime transitions and, in turn, on the gas holdup. Indeed, increasing the MEG concentration, up to its maximum value at $5\%_{wt,MEG}$, causes the *BSDs* to become narrower and unimodal shifts towards lower bubble sizes. Upon further increasing the MEG concentrations, the *BSDs* become wider and shifts towards larger bubble sizes, as highly viscous liquid phases tend to increase bubble coalescence (Deckwer, 1992; Kuncová and Zahradník, 1995; Wilkinson et al., 1992; Zahradník et al., 1997) and decreases bubble break-up rate (Shah et al., 1982; Wilkinson et al., 1992).

Such multi-scale effects are clearly observed in the local profiles. In this perspective, an insight is proposed starting from the perforated plate with $d_0$ = 0.5 mm and for the needle sparger. At low gas flow rates the local gas holdup fraction profiles are flat and are slightly wall peaked (caused by the effects described in ref. (Lucas et al., 2005)). Upon increasing the gas flow rate, the wall peak disappears and a gradient near the wall appears; upon further increasing the gas flow rate, the local gas holdup profiles become center peaked. When increasing the gas sparger openings, considering the perforated plate with $d_0$ = 1.0 mm, the local gas holdup profiles are more center packed compared with the previous case, for all the different flow rates. The local gas holdup profiles for the spider gas sparger have been presented and discussed in ref. (Besagni and Inzoli, 2016b), showing a clear poly-dispersed nature of the homogenous flow regime, being center packed for all the flow rates. In all cases, increasing the gas flowrate resulted

in overall higher void fractions and greater profile curvature from the column wall to the center, particularly after the flow regime transition. Indeed, after the transition point, the formation of "*coalescence-induced*" structures led to increased curvature of the radial profiles, where maximum local holdups occurred at the center of the column. The local gas velocity profiles are slightly specular compared with the local gas holdup profiles and the local values of the gas velocity, thus determining the gas holdup curve. In summary, there is a clear relationship between the prevailing *BSDs* and the local gas holdup profiles, which, in turn, determine the prevailing shape of the gas holdup curve owing to the imposed flow regime transitions (i.e., a gas sparger which produces a uniform bubble bed having generated *S-shaped* gas holdup curves; conversely, a gas sparger producing a poly-dispersed homogeneous flow regime that determines the monotonically increasing gas holdup curves). In this perspective, the *Ω-curves* observed for the perforated plate with $d_0$ = 0.5 mm, are clearly defined by a stable mono-dispersed homogeneous flow regime, which can stabilize all the forthcoming flow regimes by the mechanisms discussed in ref. (Lucas and Ziegenhein, 2019).

# 5 Conclusions, outlooks and perspectives

## 5.1 Conclusions

This study focuses in a specific knowledge gap and addresses it by proposing a broad and general approach to understand the bubble column fluid dynamics. Thus far, no general approach to interpret all the possible flow regimes in bubble column has been proposed and this gap has been addressed in this study by a comprehensive and unified theory, which sustains only the large-diameter assumption. The proposed theory explains that the bubble column fluid dynamics can be predicted and described by an accurate modelling of the flow regime transition points. In particular, the proposed approach states that the fluid dynamics in gas-liquid bubble columns is interpreted by a relationship—built upon flow regime transitions—between two global fluid dynamic parameters. The novel approach has been discussed and verified: to support its physical basis, we performed a comprehensive and multi-scale experimental investigation. To this end, both the global and local flow properties were experimentally studied in an gas-liquid large-scale bubble column (height of 5.3 m and inner diameter of 0.24 m and equipped with five gas spargers) that was operated in the batch mode and in counter-current mode with different *AR* values ratio, for different liquid phases. It has been shown that the proposed theory is physically grounded, that is, it is of practical significance because accurate quantification of fluid dynamics and mass transfer parameters is very important to avoid overestimations of investment costs and design failures and to develop predictive control methods. The prevailing flow

properties of bubble column fluid dynamics in different cases (i.e., changing the gas sparger design, the operation modes, *AR* and the liquid phase) were explained using the *Ω-curves*.

## 5.2 Outlooks and perspectives

The upcoming research studies should be focused on testing and verifying the proposed approach modeling the flow regime transitions as displayed in Eq. (4). In particular, coupling the present theoretical framework with the approach of Joshi and co-authors (Joshi et al., 2001), regarding stability analysis, and Ziegenhein and Lucas (Lucas and Ziegenhein, 2019), regarding bubble migration owing to the lift force, might provide a physical based method to model the operating curve which is shown in Figure 1. The flow regime transitions should be related to the prevailing system instabilities: the readers may refer to the literature of three-phase systems mentioned below as well as to refs. (Bhole and Joshi, 2005; León-Becerril et al., 2002; León-Becerril and Liné, 2001). To reach this goal an accurate modeling of bubble interfacial forces, in dense bubbly flows, is needed (which relies on the precise knowledge of the bubble size and shapes). Such closures can be derived by coupling with empirical correlations and numerical methods, as demonstrated by Besagni and Deen (Besagni and Deen, 2020), and demonstrated by Sankaranarauanan et al. (Sankaranarayanan et al., 2002), respectively.

Once the system design, the phase properties and the operation modes are known, through Eqs. (3-4) the bubble column operating curve, *Ω,* can be obtained straightforwardly; subsequently, the relationships between global and local flow properties, in the $J_T/\varepsilon_G$ coordinates (viz., in the different flow regimes), can be estimated a-priori[7] by variable formulations of the drift-flux model (Zuber and Findlay, 1965):

$$\frac{\left\langle U_G \right\rangle}{\left\langle \overline{\varepsilon_G} \right\rangle} = C_0 \left\langle \overline{U_G} + \overline{U_L} \right\rangle + C_1 \tag{15}$$

In Eq. (15), $\langle\text{-}\rangle$ denotes a spatial average, whereas $\overline{\ }$ denotes a time-average, $C_0$ is the distribution coefficient and $C_1$ is slip velocity. $C_0$ and $C_1$ summarize the local flow properties from a global point of view. Turney et al. (2018) (Turney et al., 2018) mentioned that the assumption of constant $C_0$ and $C_1$ as well as the non-time-dependent assumption lead to significant errors. The present proposal overcomes these limitations by unveiling the relationships between $C_0$ and $C_1$ and the flow conditions (viz., the $J_T/\varepsilon_G$ coordinates) as well as the time variable ($z$):

[7] Each point on the Ω-curve depicts global and local flow properties which do not depend on the phase properties, the system design and the operation modes, but they are related to the location on the Ω-curve.

$$C_0 = \zeta_i(J_T, z) \tag{16}$$

$$C_1 = \chi_i(J_T, z) \tag{17}$$

The analytical formulation displayed in Eqs. (16-17) unveils the multi-dimensional nature of the $\Omega$-curve and is the objective of future research activities. Once the local flow properties are known, the interfacial area can be computed and, finally, on the basis of mass-transfer models, the mass transfer rate can be derived.

It is expected that the present theory will answer some fundamental questions, which will help in addressing some existing discussions. This in turn, will open up a novel field of research activities, which will help in extending the theory displayed in Figure 1 to small and micro-scale systems, overcoming the large-diameter constraint, as well as to three-phase systems. In this perspective, it has not escaped our notice that the shape of the proposed curve in Figure 1 is similar to the one proposal by Owen and Hewitt (Owen, 1986) for the pressure gradient distribution (somehow related to the gas holdup in Figure 1) against dimensionless gas velocity (somehow related to the drift-flux in Figure 1) for gas–liquid flow in (small-diameter) vertical pipes (which is provided in appendix A). This might lead to a possible generalization of the proposed theory within a broader perspective. Figure 1, in the present study, may be a sub case of a more general operating curve, which also considers the slug-flow regime (whose boundaries disappear for large-diameter systems) and related instabilities. For more details the readers may refer to the flow regime transitions described by Taitel et al. (Taitel et al., 1980) and to the related instabilities discussed by (Biesheuvel and Gorissen, 1990). Extending the present theory toward smaller diameter pipes relies on the modeling of the Rayleigh-Taylor instability; in this sense the reader may refer to the linear instability theory presented by Didwania and Homsy (Didwania and Homsy, 1981b). Beside, a further generalization of the proposed approach might be to extend the present theoretical framework to three-phase systems; in this perspective, it is worth mentioning the previous literature proposed by Batchelor (Batchelor, 1988), Anderson et al. (Anderson and Jackson, 1967), Homsey and co-workers (Didwania and Homsy, 1981a, b; Didwania and Homsy, 1982; El-Kaissy and Homsy, 1976), Joshi and co-workers (Bhole and Joshi, 2005; Ghatage et al., 2014; Joshi et al., 2001; Shnip et al., 1992) and Mutsers and Rietema (Mutsers and Rietema, 1977). In these papers, solid-liquid multiphase systems have been analyzed and details regarding the stabilizing and destabilizing forces and instabilities are described. As stated for small-diameter pipes, the proposed theory may be a particular case of multi-phase systems; in this case, there will be a simultaneous effect of hydrodynamic and non-hydrodynamic stresses, as mentioned in ref. (Sundaresan, 2003) for the case of fluidized bed.

Thus, Figure 1, may be a sub-case of a more general operating curve, which also considers a third phase. To summarize, future studies should be focused on re-drawing Figure 1 for small and large diameter pipes for two- and three-phase systems. Once the general shape is derived, force balances should be performed to determine the analytical formulation of the different flow regime transition points. Then, the flow regime properties should be derived using Eqs. (15-17).

# 6 APPENDIX A

Figure 18 displays the pressure gradient distribution against dimensionless gas velocity for gas–liquid flow in (small-diameter) vertical pipes (Owen, 1986).

**Declaration of interests**

☒ The authors declare that they have no known competing financial interests or personal relationships that could have appeared to influence the work reported in this paper.

☐The authors declare the following financial interests/personal relationships which may be considered as potential competing interests:

# Credit authorship contribution statement

**Giorgio Besagni:** Conceptualization, Data curation, Formal analysis, Investigation, Methodology, Visualization, Writing - original draft, Writing - review & editing.

# 7 REFERENCES

Akita, K., Yoshida, F., 1973. Gas Holdup and Volumetric Mass Transfer Coefficient in Bubble Columns. Effects of Liquid Properties. Industrial & Engineering Chemistry Process Design and Development 12, 76-80.

Anderson, J.L., Quinn, J.A., 1970. Bubble columns: flow transitions in the presence of trace contaminants. Chemical Engineering Science 25, 373-380.

Anderson, T.B., Jackson, R., 1967. Fluid Mechanical Description of Fluidized Beds. Equations of Motion. Industrial & Engineering Chemistry Fundamentals 6, 527-539.

Barbosa, J.R., Govan, A.H., Hewitt, G.F., 2001. Visualisation and modelling studies of churn flow in a vertical pipe. International Journal of Multiphase Flow 27, 2105-2127.

Barrau, E., Rivière, N., Poupot, C., Cartellier, A., 1999. Single and double optical probes in air-water two-phase flows: real time signal processing and sensor performance. International Journal of Multiphase Flow 25, 229-256.

Batchelor, G.K., 1988. A new theory of the instability of a uniform fluidized bed. Journal of Fluid Mechanics 193, 75-110.

Besagni, G., Deen, N.G., 2020. Aspect ratio of bubbles in different liquid media: A novel correlation. Chemical Engineering Science 215, 115383.

Besagni, G., Gallazzini, L., Inzoli, F., 2019. On the scale-up criteria for bubble columns. Petroleum 5, 114-122.

Besagni, G., Inzoli, F., 2019. Bubble sizes and shapes in a counter-current bubble column with pure and binary liquid phases. Flow Measurement and Instrumentation 67, 55-82.

Besagni, G., Inzoli, F., Ziegenhein, T., 2018b. Two-phase bubble columns: A comprehensive review. ChemEngineering 2, 13.

Besagni, G., Di Pasquali, A., Gallazzini, L., Gottardi, E., Colombo, L.P.M., Inzoli, F., 2017a. The effect of aspect ratio in counter-current gas-liquid bubble columns: Experimental results and gas holdup correlations. International Journal of Multiphase Flow 94, 53-78.

Besagni, G., Inzoli, F., De Guido, G., Pellegrini, L.A., 2017b. The dual effect of viscosity on bubble column hydrodynamics. Chemical Engineering Science 158, 509-538.

Besagni, G., Inzoli, F., 2017. The effect of liquid phase properties on bubble column fluid dynamics: Gas holdup, flow regime transition, bubble size distributions and shapes, interfacial areas and foaming phenomena. Chemical Engineering Science 170, 270-296.

Besagni, G., Gallazzini, L., Inzoli, F., 2018a. Effect of gas sparger design on bubble column hydrodynamics using pure and binary liquid phases. Chemical Engineering Science 176, 116-126.

Besagni, G., Inzoli, F., 2016a. Bubble size distributions and shapes in annular gap bubble column. Experimental Thermal and Fluid Science 4, 27–48.

Besagni, G., Inzoli, F., 2016b. Comprehensive experimental investigation of counter-current bubble column hydrodynamics: Holdup, flow regime transition, bubble size distributions and local flow properties. Chemical Engineering Science 146, 259-290.

Besagni, G., Inzoli, F., 2016c. Influence of internals on counter-current bubble column hydrodynamics: Holdup, flow regime transition and local flow properties. Chemical Engineering Science 145, 162-180.

Besagni, G., Inzoli, F., De Guido, G., Pellegrini, L.A., 2016. Experimental investigation on the influence of ethanol on bubble column hydrodynamics. Chemical Engineering Research and Design 112, 1-15.

Besagni, G., Inzoli, F., 2015. Influence of electrolyte concentration on holdup, flow regime transition and local flow properties in a large scale bubble column. Journal of Physics: Conference Series 655, 012039.

Bhole, M.R., Joshi, J.B., 2005. Stability analysis of bubble columns: Predictions for regime transition. Chemical Engineering Science 60, 4493-4507.

Biesheuvel, A., Gorissen, W.C.M., 1990. Void fraction disturbances in a uniform bubbly fluid. International Journal of Multiphase Flow 16, 211-231.

Brooks, C.S., Paranjape, S.S., Ozar, B., Hibiki, T., Ishii, M., 2012. Two-group drift-flux model for closure of the modified two-fluid model. International Journal of Heat and Fluid Flow 37, 196-208.

Deckwer, W., Graeser, U., Langemann, H., Serpemen, Y., 1973. Zones of different mixing in the liquid phase of bubble columns. Chemical Engineering Science 28, 1223-1225.

Deckwer, W.D., 1992. Bubble column reactors. Wiley.

Di Marco, P., 2005. Birth, life and death of gas bubbles rising in a stagnant liquid. International Journal of Heat and Technology 23, 17-26.

Didwania, A.K., Homsy, G.M., 1981a. Flow regimes and flow transitions in liquid fluidized beds. International Journal of Multiphase Flow 7, 563-580.

Didwania, A.K., Homsy, G.M., 1981b. Rayleigh-Taylor instabilities in fluidized beds. Industrial & Engineering Chemistry Fundamentals 20, 318-323.

Didwania, A.K., Homsy, G.M., 1982. Resonant sideband instabilities in wave propagation in fluidized beds. Journal of Fluid Mechanics 122, 433-438.

Domingos, P., 1999. The Role of Occam's Razor in Knowledge Discovery. Data Mining and Knowledge Discovery 3, 409-425.

El-Kaissy, M.M., Homsy, G.M., 1976. Instability waves and the origin of bubbles in fluidized beds: Part 1: Experiments. International Journal of Multiphase Flow 2, 379-395.

Gaddis, E.S., Vogelpohl, A., 1986. Bubble formation in quiescent liquids under constant flow conditions. Chemical Engineering Science 41, 97-105.

Ghatage, S.V., Bhole, M.R., Padhiyar, N., Joshi, J.B., Evans, G.M., 2014. Prediction of regime transition in three-phase sparged reactors using linear stability analysis. Chemical Engineering Journal 235, 307-330.

Guo, K., Wang, T., Yang, G., Wang, J., 2017. Distinctly different bubble behaviors in a bubble column with pure liquids and alcohol solutions. Journal of Chemical Technology & Biotechnology 92, 432-441.

Hewitt, G.F.M., C.J.; Wilkes, N.S., 1985. Experimental and modelling studies of annular flow in the region between flow reversal and the pressure drop minimum. PCH Physicochem. Hydrodyn 6, 69-86.

Hills, J.H., 1976. The operation of a bubble column at high throughputs: I. Gas holdup measurements. The Chemical Engineering Journal 12, 89-99.

Jin, H., Lian, Y., Yang, S., He, G., Guo, Z., 2013. The parameters measurement of air–water two phase flow using the electrical resistance tomography (ERT) technique in a bubble column. Flow Measurement and Instrumentation 31, 55-60.

Joshi, J.B., Deshpande, N.S., Dinkar, M., Phanikumar, D.V., 2001. Hydrodynamic stability of multiphase reactors, Advances in Chemical Engineering. Academic Press, pp. 1-130.

Kang, Y., Cho, Y.J., Woo, K.J., Kim, K.I., Kim, S.D., 2000. Bubble properties and pressure fluctuations in pressurized bubble columns. Chemical Engineering Science 55, 411-419.

Kitscha, J., Kocamustafaogullari, G., 1989. Breakup criteria for fluid particles. International Journal of Multiphase Flow 15, 573-588.

Koetsier, W.T., Van Swaaij, W.P.M., Van Der Most, M., 1976. Maximum gas holdup in bubble columns. Journal of Chemical Engineering of Japan 9, 332-333.

Kuncová, G., Zahradník, J., 1995. Gas holdup and bubble frequency in a bubble column reactor containing viscous saccharose solutions. Chemical Engineering and Processing: Process Intensification 34, 25-34.

León-Becerril, E., Cockx, A., Liné, A., 2002. Effect of bubble deformation on stability and mixing in bubble columns. Chemical Engineering Science 57, 3283-3297.

León-Becerril, E., Liné, A., 2001. Stability analysis of a bubble column. Chemical Engineering Science 56, 6135-6141.

Lima, V.N., Rodrigues, C.S.D., Borges, R.A.C., Madeira, L.M., 2018. Gaseous and liquid effluents treatment in bubble column reactors by advanced oxidation processes: A review. Critical Reviews in Environmental Science and Technology 48, 949-996.

Lin, T.-J., Reese, J., Hong, T., Fan, L.-S., 1996. Quantitative analysis and computation of two-dimensional bubble columns. AIChE Journal 42, 301-318.

Lucas, D., Krepper, E., Liao, Y., Rzehak, R., Ziegenhein, T., 2020. General guideline for closure model development for gas-liquid flows in the multi-fluid framework. Nuclear Engineering and Design 357, 110396.

Lucas, D., Prasser, H.M., Manera, A., 2005. Influence of the lift force on the stability of a bubble column. Chemical Engineering Science 60, 3609-3619.

Lucas, D., Ziegenhein, T., 2019. Influence of the bubble size distribution on the bubble column flow regime. International Journal of Multiphase Flow 120, 103092.

Magnaudet, J., Eames, I., 2000. The Motion of High-Reynolds-Number Bubbles in Inhomogeneous Flows. Annual Review of Fluid Mechanics 32, 659-708.

Manjrekar, O.N., Dudukovic, M.P., 2019. Identification of flow regime in a bubble column reactor with a combination of optical probe data and machine learning technique. Chemical Engineering Science: X 2, 100023.

Maruyama, T., Yoshida, S., Mizushina, T., 1981. The flow transition in a bubble column. Journal of Chemical Engineering of Japan 14, 352-357.

Moleurs, O., Kurtin, M., 1985. Hydrodynamics of bubble columns in the uniform bubbling regime. Chemical Engineering Science 40, 647-652.

Monahan, S.M., Vitankar, V.S., Fox, R.O., 2005. CFD predictions for flow-regime transitions in bubble columns. AIChE Journal 51, 1897-1923.

Montoya, G., Lucas, D., Baglietto, E., Liao, Y., 2016. A review on mechanisms and models for the churn-turbulent flow regime. Chemical Engineering Science 141, 86-103.

Mudde, R.F., 2005. Gravity-driven bubbly flows. Annual Review of Fluid Mechanics 37, 393-423.

Mudde, R.F., Harteveld, W.K., van den Akker, H.E.A., 2009. Uniform Flow in Bubble Columns. Industrial & Engineering Chemistry Research 48, 148-158.

Muroyama, K., Imai, K., Oka, Y., Hayashi, J.i., 2013. Mass transfer properties in a bubble column associated with micro-bubble dispersions. Chemical Engineering Science 100, 464-473.

Mutsers, S.M.P., Rietema, K., 1977. The effect of interparticle forces on the expansion of a homogeneous gas-fluidized bed. Powder Technology 18, 239-248.

Nedeltchev, S., 2015. New methods for flow regime identification in bubble columns and fluidized beds. Chemical Engineering Science 137, 436-446.

Nedeltchev, S., 2020. Precise identification of the end of the gas maldistribution in bubble columns equipped with perforated plate gas distributors. Chemical Engineering Journal 386, 121535.

Olmos, E., Gentric, C., Poncin, S., Midoux, N., 2003. Description of flow regime transitions in bubble columns via laser Doppler anemometry signals processing. Chemical Engineering Science 58, 1731-1742.

Orvalho, S., Hashida, M., Zednikova, M., Stanovsky, P., Ruzicka, M.C., Sasaki, S., Tomiyama, A., 2018. Flow regimes in slurry bubble column: Effect of column height and particle concentration. Chemical Engineering Journal 351, 799-815.

Owen, D.G.H., G.F., 1986. An improved annular two-phase flow model (Paper C1), Third International Conference on Multiphase Flow, The Hague, Netherlands.

Patil, V.K., Joshi, J.B., Sharma, M.M., 1984. Sectionalised bubble column: Gas hold-up and wall side solid—Liquid mass transfer coefficient. The Canadian Journal of Chemical Engineering 62, 228-232.

Prosperetti, A., 2004. Bubbles. Physics of Fluids 16, 1852-1865.

Reilly, I., Scott, D., Debruijn, T., MacIntyre, D., 1994. The role of gas phase momentum in determining gas holdup and hydrodynamic flow regimes in bubble column operations. The Canadian Journal of Chemical Engineering 72, 3-12.

Reilly, I.G., Scott, D.S., De Bruijn, T., Jain, A., Piskorz, J., 1986. A correlation for gas holdup in turbulent coalescing bubble columns. The Canadian Journal of Chemical Engineering 64, 705-717.

Ribeiro, C.P., 2008. On the estimation of the regime transition point in bubble columns. Chemical Engineering Journal 140, 473-482.

Ribeiro Jr, C.P., Mewes, D., 2007. The influence of electrolytes on gas hold-up and regime transition in bubble columns. Chemical Engineering Science 62, 4501-4509.

Risso, F., 2018. Agitation, Mixing, and Transfers Induced by Bubbles. Annual Review of Fluid Mechanics 50, 25-48.

Rollbusch, P., Becker, M., Ludwig, M., Bieberle, A., Grünewald, M., Hampel, U., Franke, R., 2015a. Experimental investigation of the influence of column scale, gas density and liquid properties on gas holdup in bubble columns. International Journal of Multiphase Flow 75, 88-106.

Rollbusch, P., Bothe, M., Becker, M., Ludwig, M., Grünewald, M., Schlüter, M., Franke, R., 2015b. Bubble columns operated under industrially relevant conditions – Current understanding of design parameters. Chemical Engineering Science 126, 660-678.

Ruzicka, M.C., Drahovs, J., Fialova, M., Thomas, N.H., 2001a. Effect of bubble column dimensions on flow regime transition. Chemical Engineering Science 56, 6117-6124.

Ruzicka, M.C., Zahradník, J., Drahoš, J., Thomas, N.H., 2001b. Homogeneous–heterogeneous regime transition in bubble columns. Chemical Engineering Science 56, 4609-4626.

Sankaranarayanan, K., Shan, X., Kevrekidis, I.G., Sundaresan, S., 2002. Analysis of drag and virtual mass forces in bubbly suspensions using an implicit formulation of the lattice Boltzmann method. Journal of Fluid Mechanics 452, 61-96.

Sasaki, S., Hayashi, K., Tomiyama, A., 2016. Effects of liquid height on gas holdup in air–water bubble column. Experimental Thermal and Fluid Science 72, 67-74.

Sasaki, S., Uchida, K., Hayashi, K., Tomiyama, A., 2017. Effects of column diameter and liquid height on gas holdup in air-water bubble columns. Experimental Thermal and Fluid Science 82, 359-366.

Schumpe, A., Grund, G., 1986. The gas disengagement technique for studying gas holdup structure in bubble columns. The Canadian Journal of Chemical Engineering 64, 891-896.

Shah, Y.T., Joseph, S., Smith, D.N., Ruether, J.A., 1985. Two-bubble class model for churn turbulent bubble-column reactor. Industrial & Engineering Chemistry Process Design and Development 24, 1096-1104.

Shah, Y.T., Kelkar, B.G., Godbole, S.P., Deckwer, W.-D., 1982. Design parameters estimations for bubble column reactors. AIChE Journal 28, 353-379.

Shaikh, A., Al-Dahhan Muthanna, H., 2007. A Review on Flow Regime Transition in Bubble Columns, International Journal of Chemical Reactor Engineering.

Sharaf, S., Zednikova, M., Ruzicka, M.C., Azzopardi, B.J., 2016. Global and local hydrodynamics of bubble columns – Effect of gas distributor. Chemical Engineering Journal 288, 489-504.

Shnip, A.I., Kolhatkar, R.V., Swamy, D., Joshi, J.B., 1992. Criteria for the transition from the homogeneous to the heterogeneous regime in two-dimensional bubble column reactors. International Journal of Multiphase Flow 18, 705-726.

Sundaresan, S., 2003. Instabilities in Fluidized Beds. Annual Review of Fluid Mechanics 35, 63-88.

Taitel, Y., Bornea, D., Dukler, A.E., 1980. Modelling flow pattern transitions for steady upward gas-liquid flow in vertical tubes. AIChE Journal 26, 345-354.

Takagi, S., Matsumoto, Y., 2011. Surfactant effects on bubble motion and bubbly flows. Annual Review of Fluid Mechanics 43, 615-636.

Takagi, S., Ogasawara, T., Matsumoto, Y., 2008. The effects of surfactant on the multiscale structure of bubbly flows. Philosophical Transactions of the Royal Society A: Mathematical, Physical and Engineering Sciences 366, 2117-2129.

Thorat, B.N., Shevade, A.V., Bhilegaonkar, K.N., Aglawe, R.H., Parasu Veera, U., Thakre, S.S., Pandit, A.B., Sawant, S.B., Joshi, J.B., 1998. Effect of Sparger Design and Height to Diameter Ratio on Fractional Gas Hold-up in Bubble Columns. Chemical Engineering Research and Design 76, 823-834.

Turney, D.E., Kalaga, D.V., Ansari, M., Yakobov, R., Joshi, J.B., 2018. Reform of the drift-flux model of multiphase flow in pipes, wellbores, and reactor vessels. Chemical Engineering Science 184, 251-258.

Wallis, G.B., 1969. One-dimensional two-phase flow.

Wilkinson, P.M., Spek, A.P., van Dierendonck, L.L., 1992. Design Parameters Estimation for Scale-Up of High-Pressure Bubble Columns. A.I.Ch.E. Journal 38, 544-554.

Xue, J., Al-Dahhan, M., Dudukovic, M.P., Mudde, R.F., 2008. Bubble velocity, size, and interfacial area measurements in a bubble column by four-point optical probe. AIChE Journal 54, 350-363.

Yoshida, F., Akita, K., 1965. Performance of gas bubble columns: Volumetric liquid-phase mass transfer coefficient and gas holdup. AIChE Journal 11, 9-13.

Zahradník, J., Fialová, M., Linek, V., 1999. The effect of surface-active additives on bubble coalescence in aqueous media. Chemical Engineering Science 54, 4757-4766.

Zahradník, J., Fialová, M., Ruzicka, M., Drahoš, J., Kastanek, F., Thomas, N.H., 1997. Duality of the gas--liquid flow regimes in bubble column reactors. Chemical Engineering Science 52, 3811-3826.

Ziegenhein, T., Lucas, D., 2019. The critical bubble diameter of the lift force in technical and environmental, buoyancy-driven bubbly flows. International Journal of Multiphase Flow 116, 26-38.

Ziegenhein, T., Lucas, D., Besagni, G., Inzoli, F., 2020. Experimental study of the liquid velocity and turbulence in a large-scale air-water counter-current bubble column. Experimental Thermal and Fluid Science 111, 109955.

Zuber, N., Findlay, J.A., 1965. Average Volumetric Concentration in Two-Phase Flow Systems. Journal of Heat Transfer 87, 453-468.

## Figure Captions

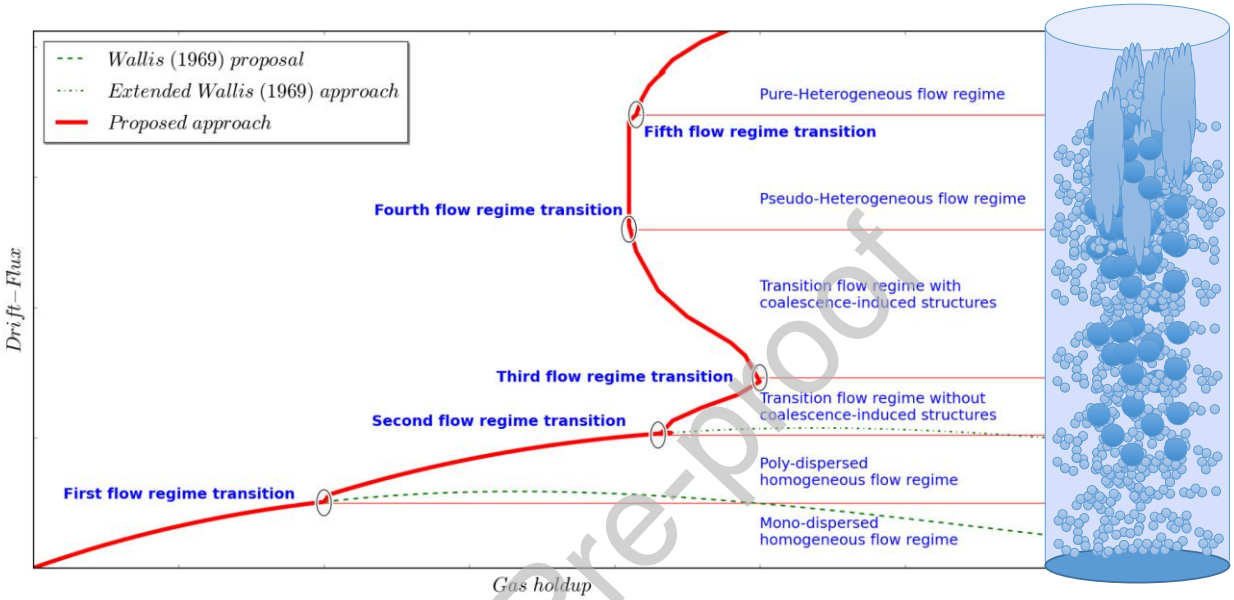


**Figure 1.** *Anatomy of bubble column flow regime and flow regime transitions. In the graphical representation of bubble column, on the right, each vertical position represents a time-averaged condition for a fixed drift-flux value.*

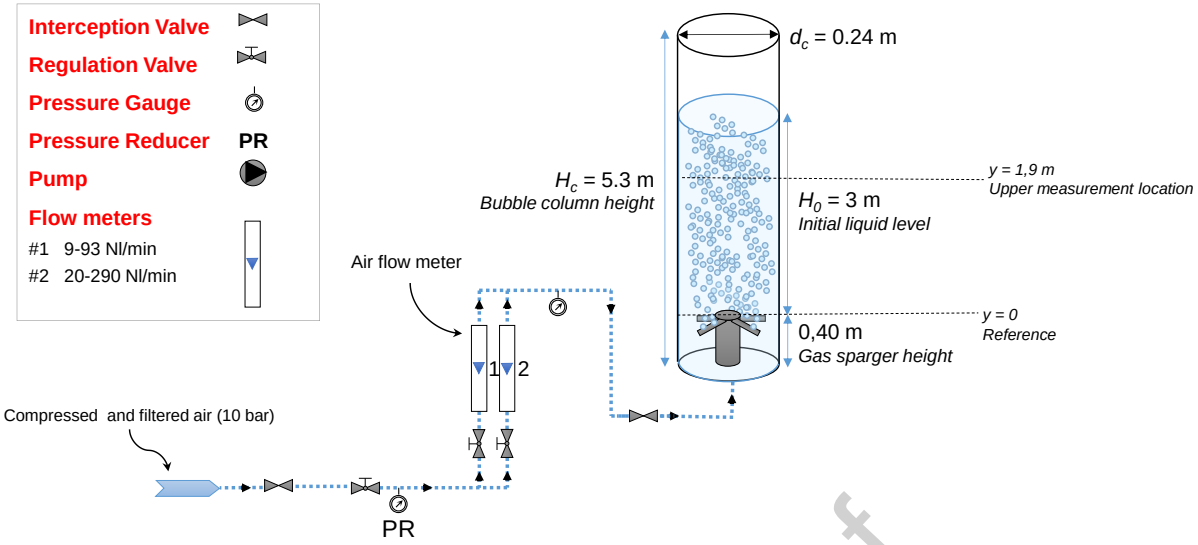


**Figure 2.** *The experimental setup.*

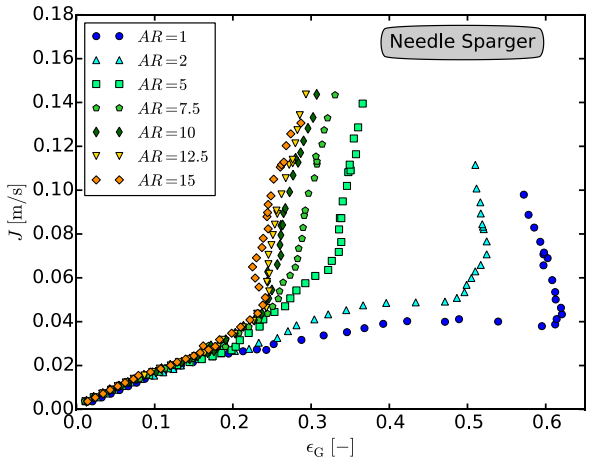


(a) Needle sparger in the batch mode

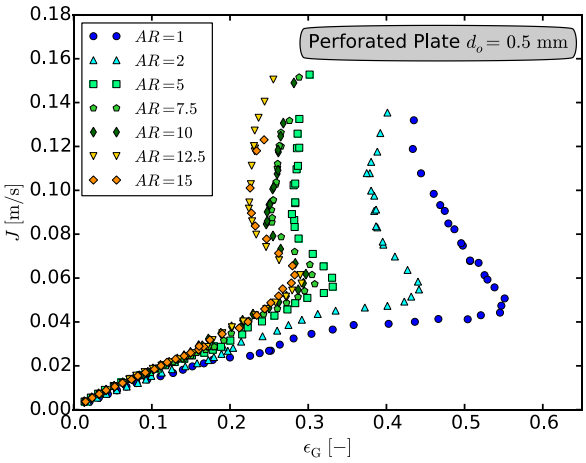


(b) Perforated plate ($d_o$ = 0.5 mm) in the batch mode

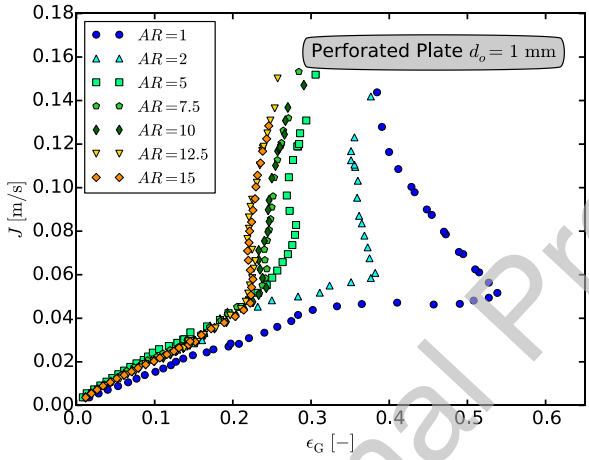


(c) Perforated plate ($d_o$ = 1.0 mm) in the batch mode

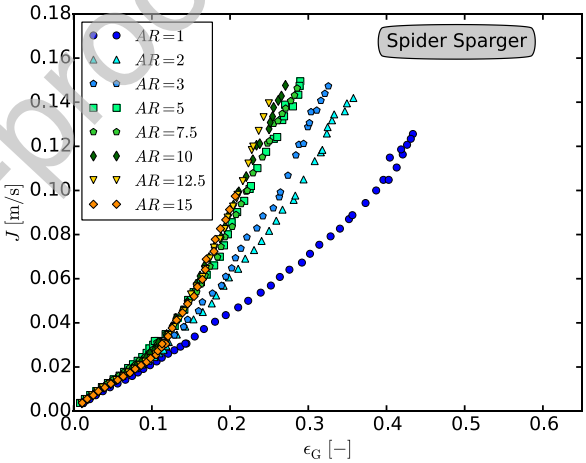


(d) Spider sparger in the batch mode

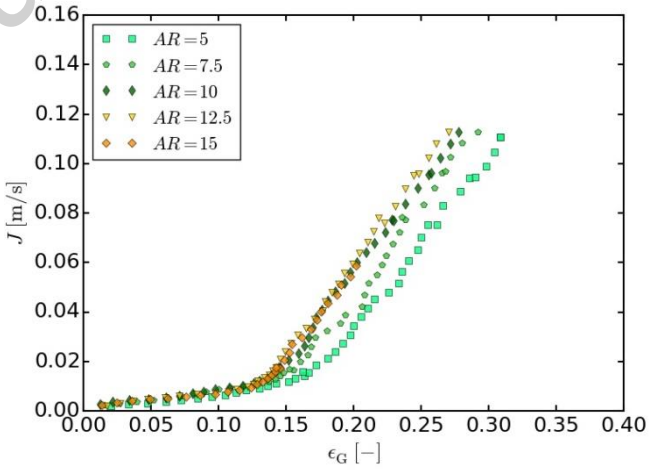


(c) Spider sparger in counter-current mode ($U_L$ = -0.0846 m/s)

**Figure 3.** *Influence of the gas sparger and AR (air-water): Ω-curves.*

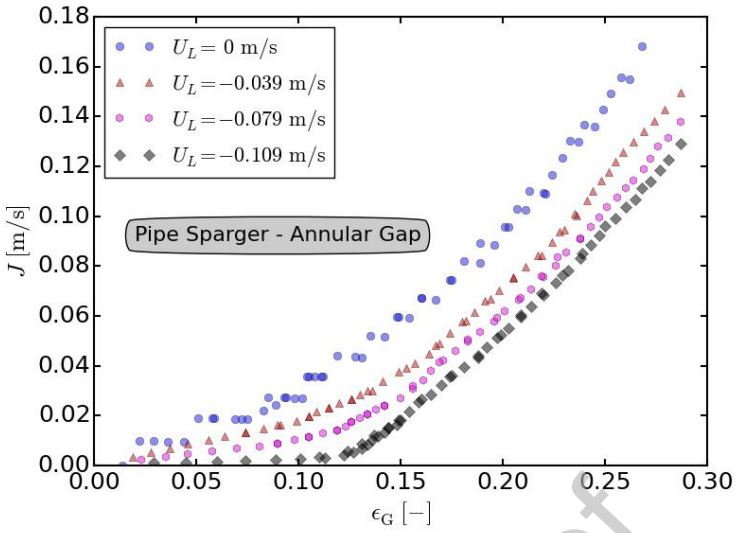


**(a) Pipe sparger in the annular gap configuration (*AR* = 12.5)**

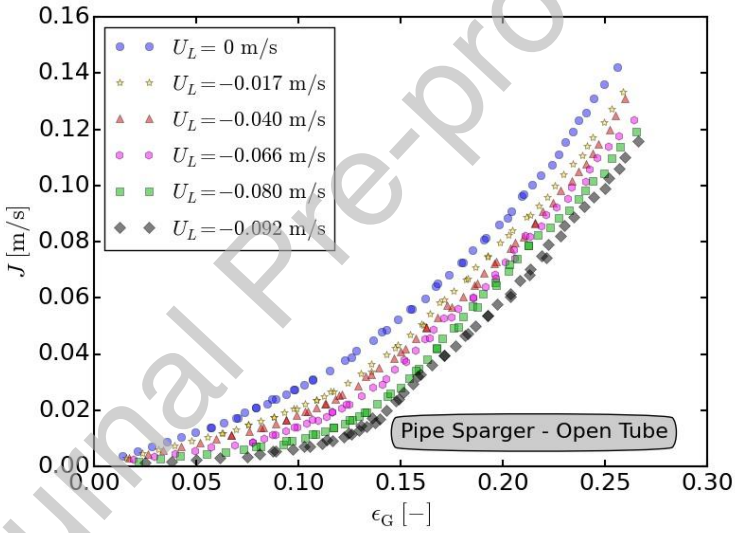


**(b) Pipe sparger in the open tube configuration (*AR* = 12.5)**

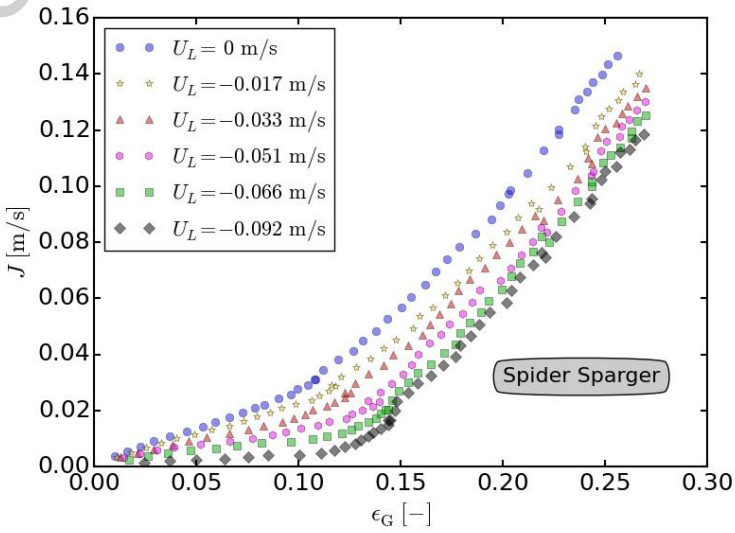


**(c) Spider sparger (*AR* = 12.5)**

**Figure 4.** *Influence of the operation mode and $U_L$ (air-water): Ω-curves.*

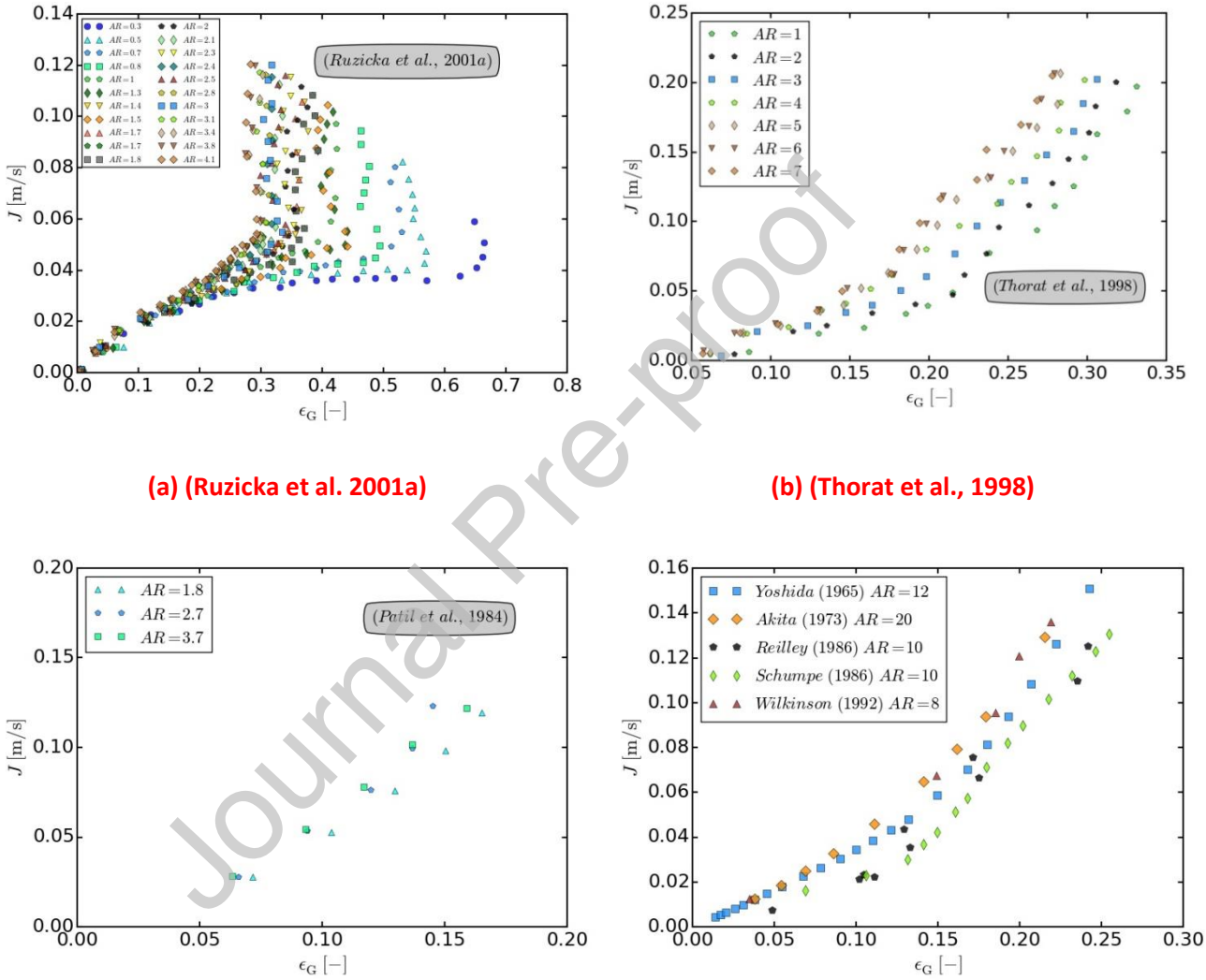


**(a) (Ruzicka et al. 2001a)** **(b) (Thorat et al., 1998)**

**(c) (Patil et al., 1984)** **(d) Other studies**

**Figure 5.** *Ω-curves derived from literature studies – part a (Table 1).*

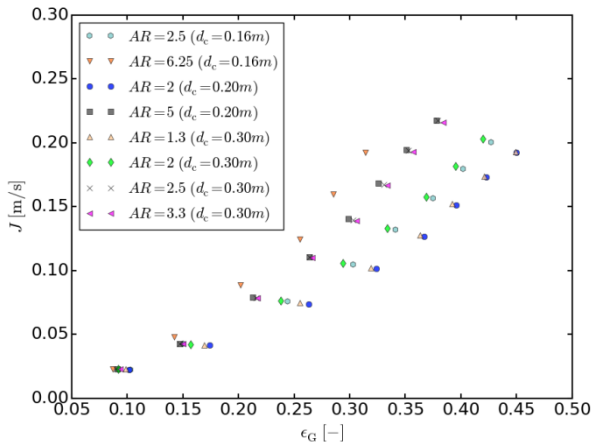


(a) (Sasaki et al., 2017) – $d_c$ < 2 m

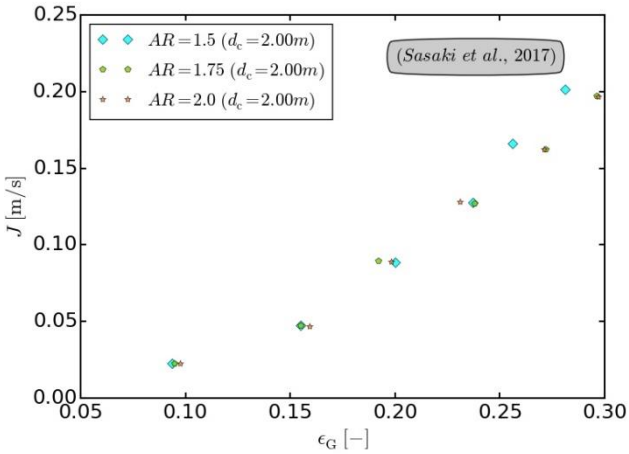


(b) (Sasaki et al., 2017) – $d_c$ = 2 m

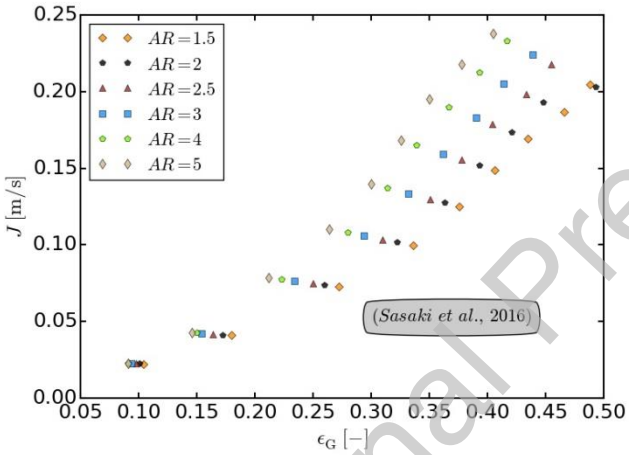


(c) (Sasaki et al., 2016)

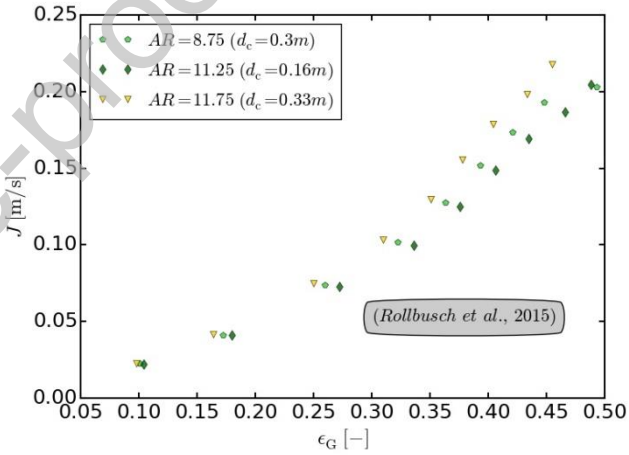


(d) (Rollbusch et al., 2015)



**Figure 6** *Ω-curves derived from literature studies – part b (Table 1).*

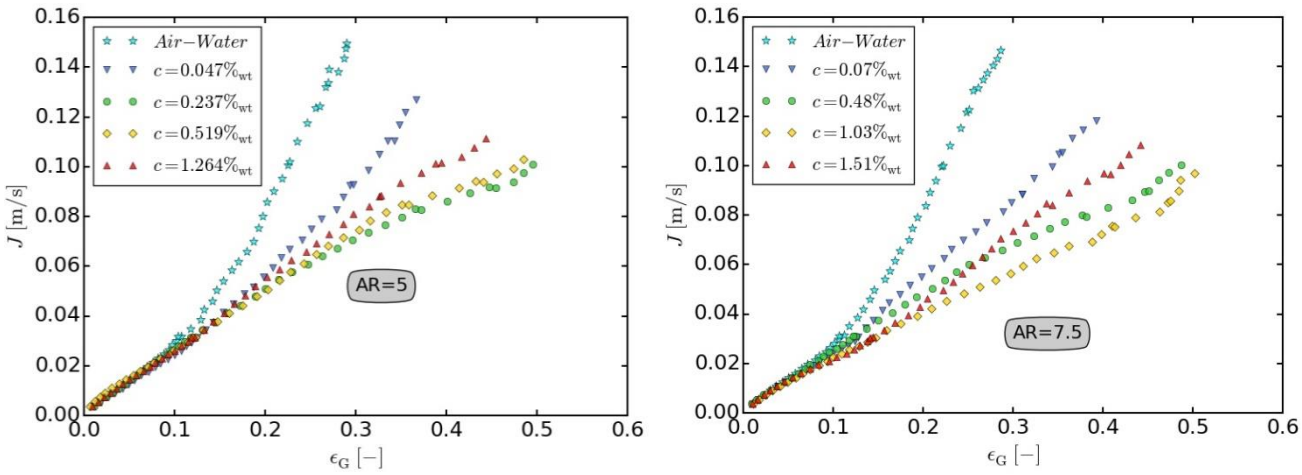


(a) AR = 5

(b) AR = 7.5

**Figure 7.** *Ω-curves for the spiger sparger operated with EtOH-water mixtures.*

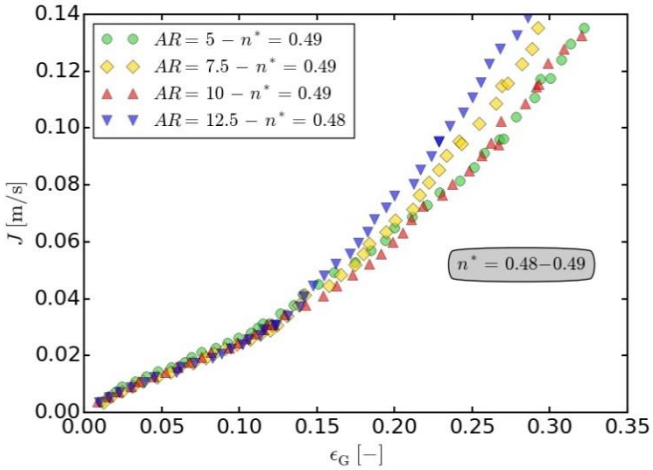


(a) n* = 0.48 – 0.49

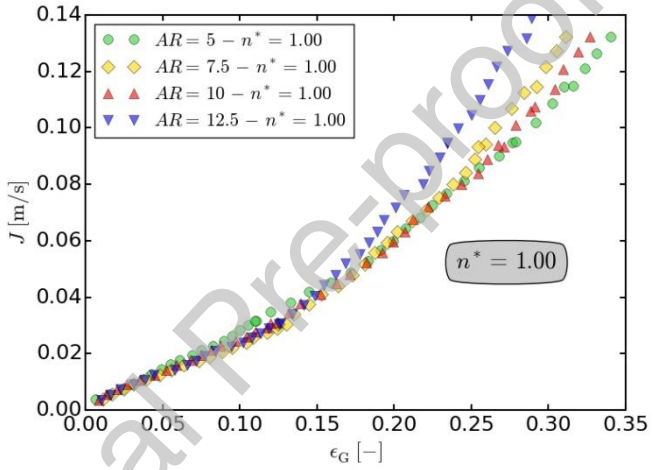


(b) n* = 1.00

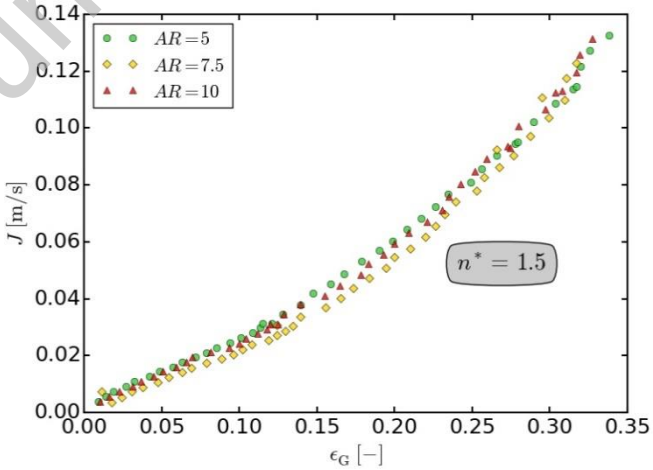


(c) n* = 1.5



**Figure 8.** *Ω-curves for the spiger sparger operated with NaCl-water mixtures.*

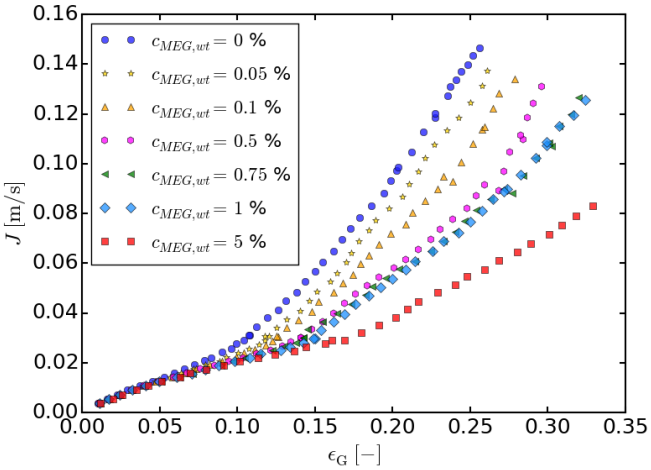


(a) Spider sparger bubble column – "*low viscosities*"

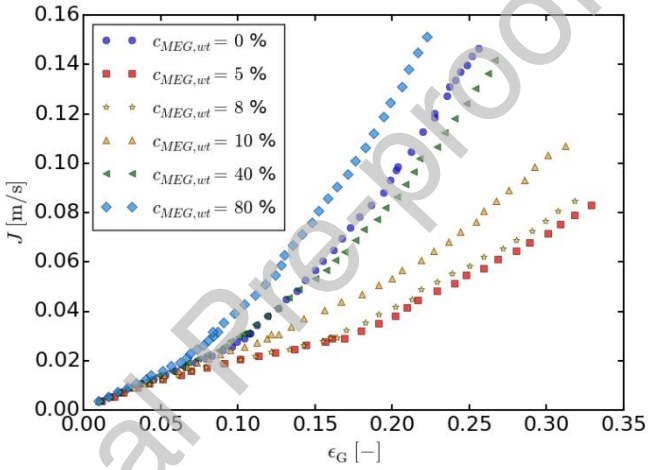


(b) Spider sparger bubble column – "*high viscosities*"

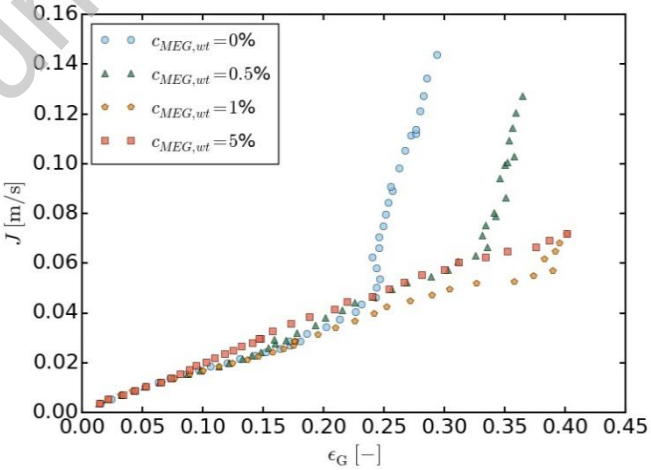


(c) Needed sparger bubble column

**Figure 9.** *Ω-curves for the spiger sparger and needle sparger operated with MEG-water mixtures.*

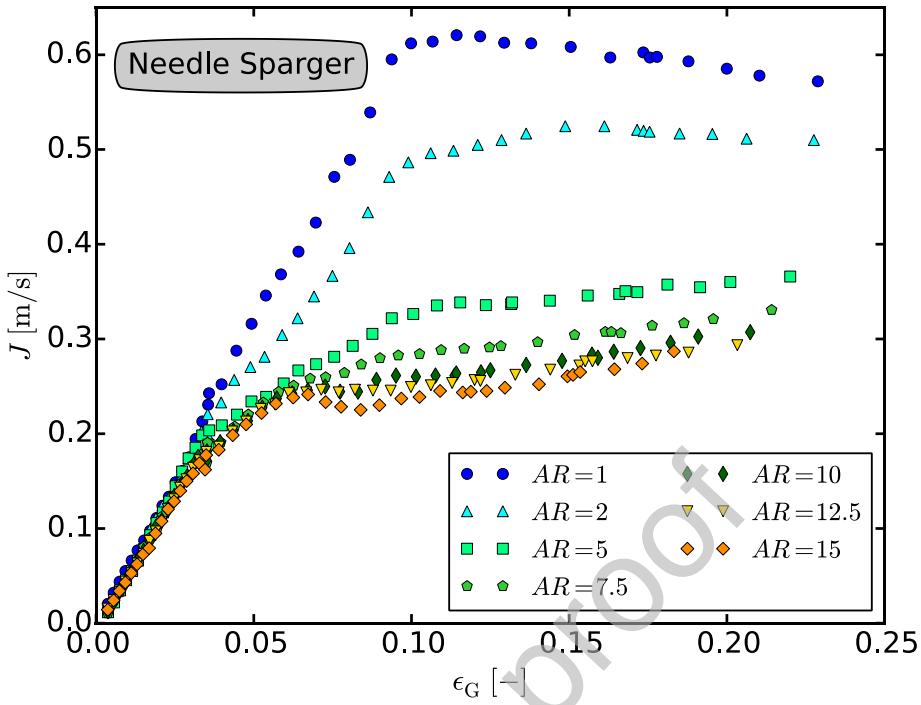


**Figure 10.** *Gas holdup curves for the needle gas sparger.*

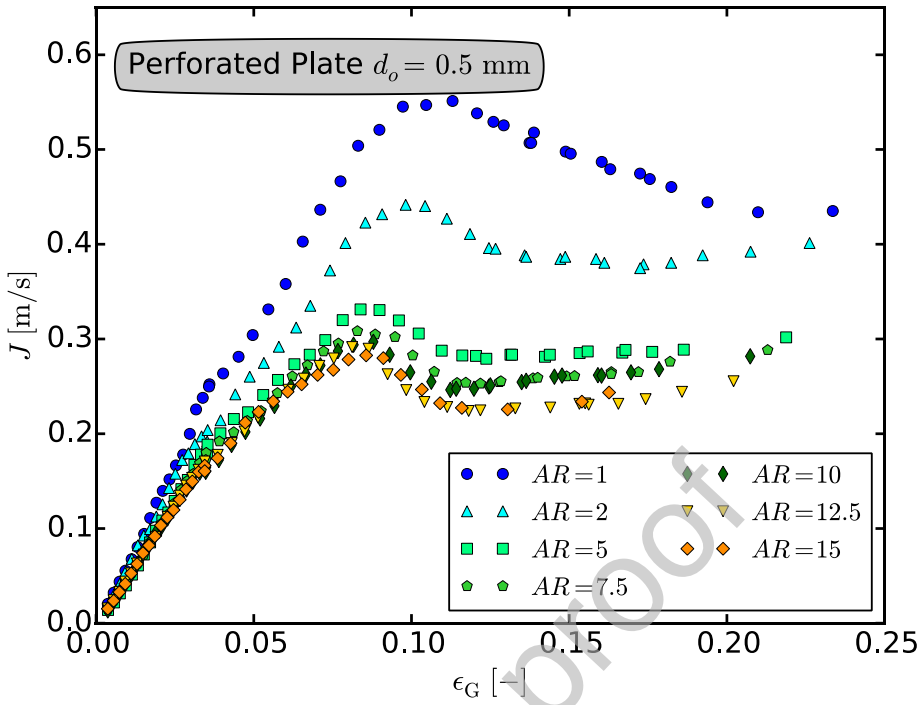


**Figure 11.** *Gas holdup curves for the perforated plate ($d_0$ = 0.5 mm) gas sparger.*

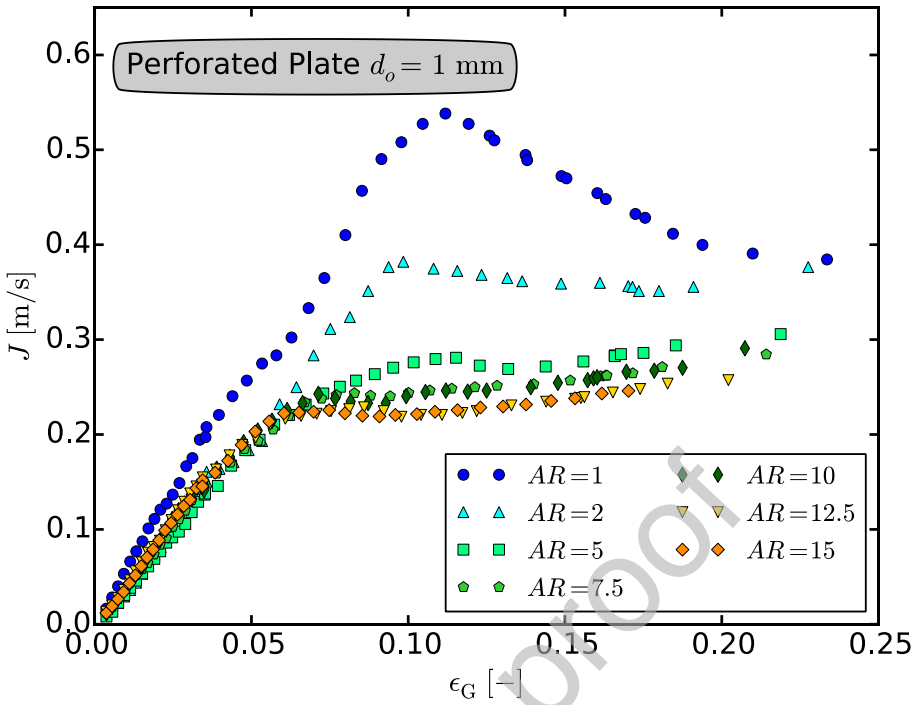


**Figure 12.** *Gas holdup curves for the perforated plate ($d_0$ = 1.0 mm) gas sparger.*

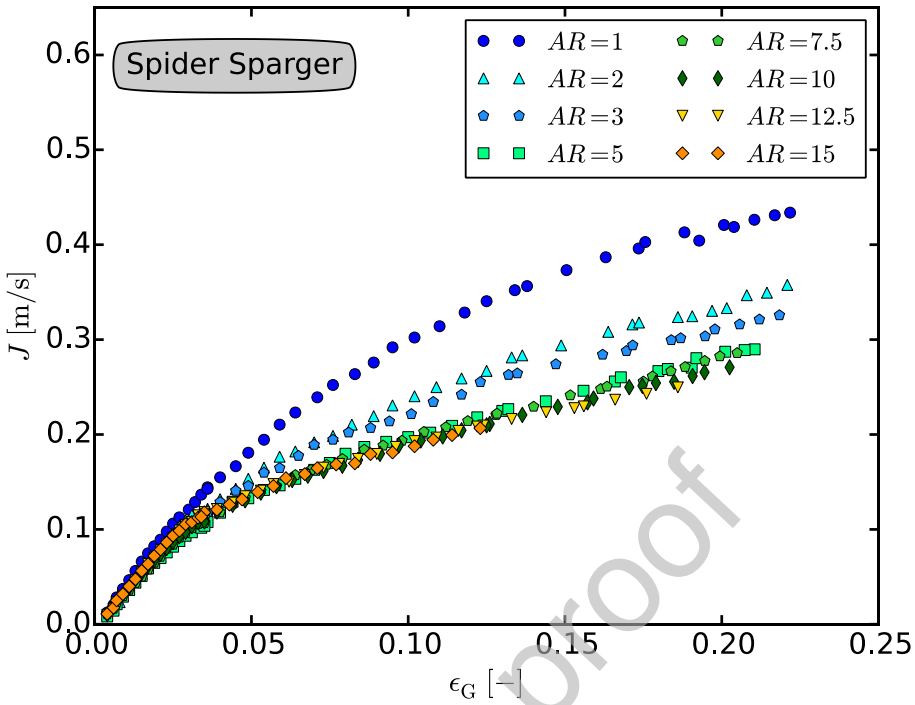


**Figure 13.** *Gas holdup curves for the spider gas sparger.*

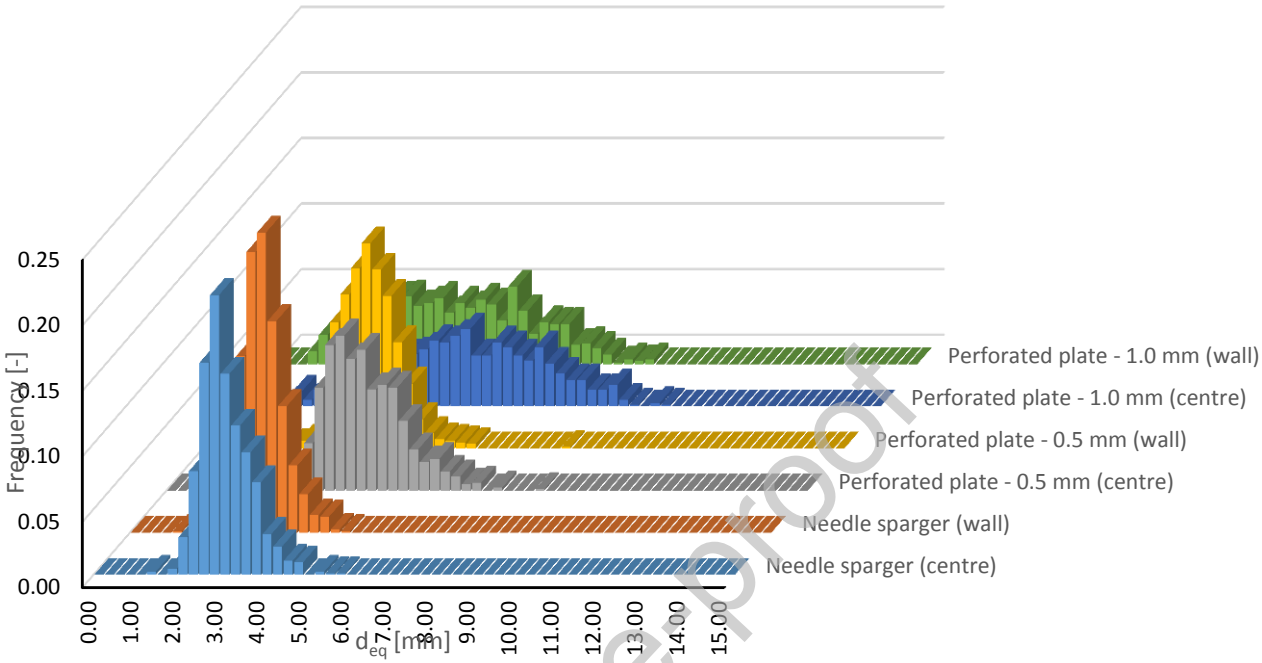


*(a) $U_G$ = 0.017 m/s*

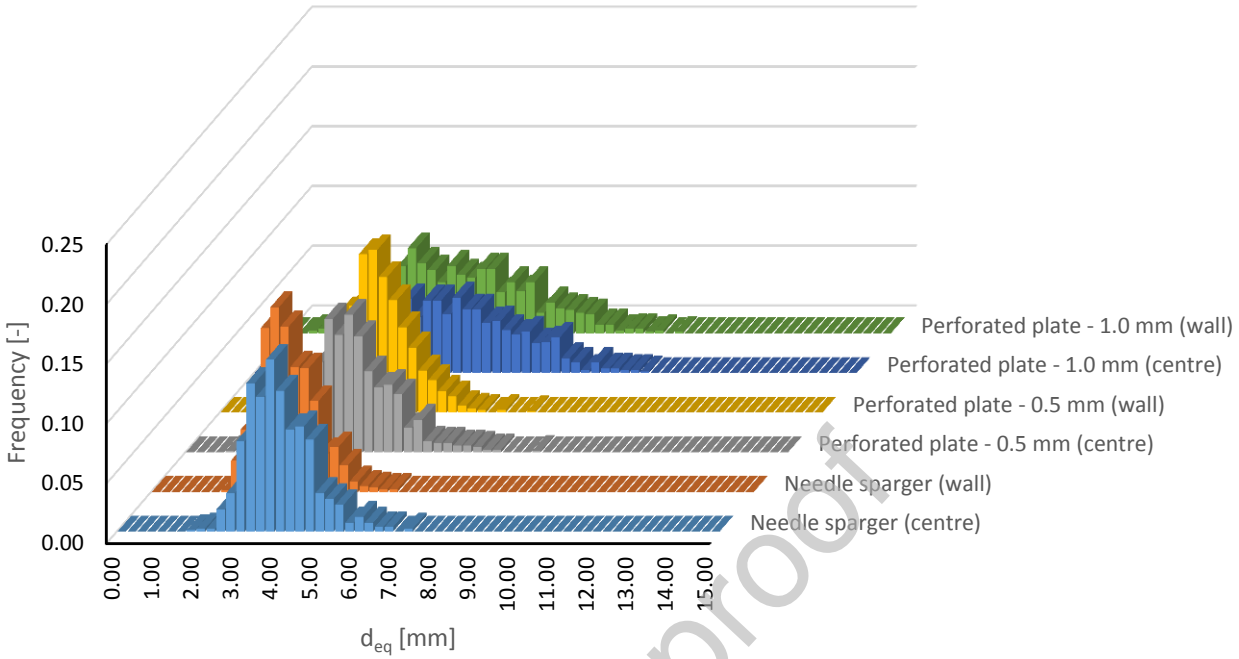


*(b) $U_G$ = 0.034 m/s*

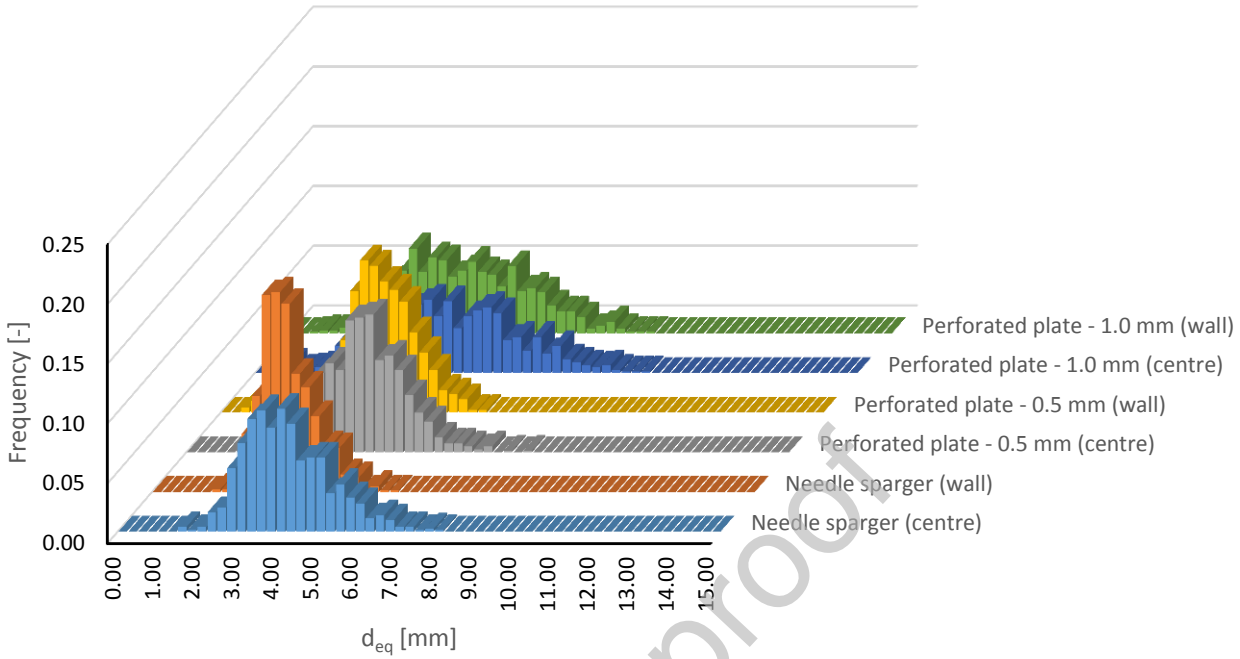


*(c) $U_G$ = 0.055 m/s*

**Figure 14.** *Bubble size distributions for the different gas spargers AR = 12.5) – batch mode.*

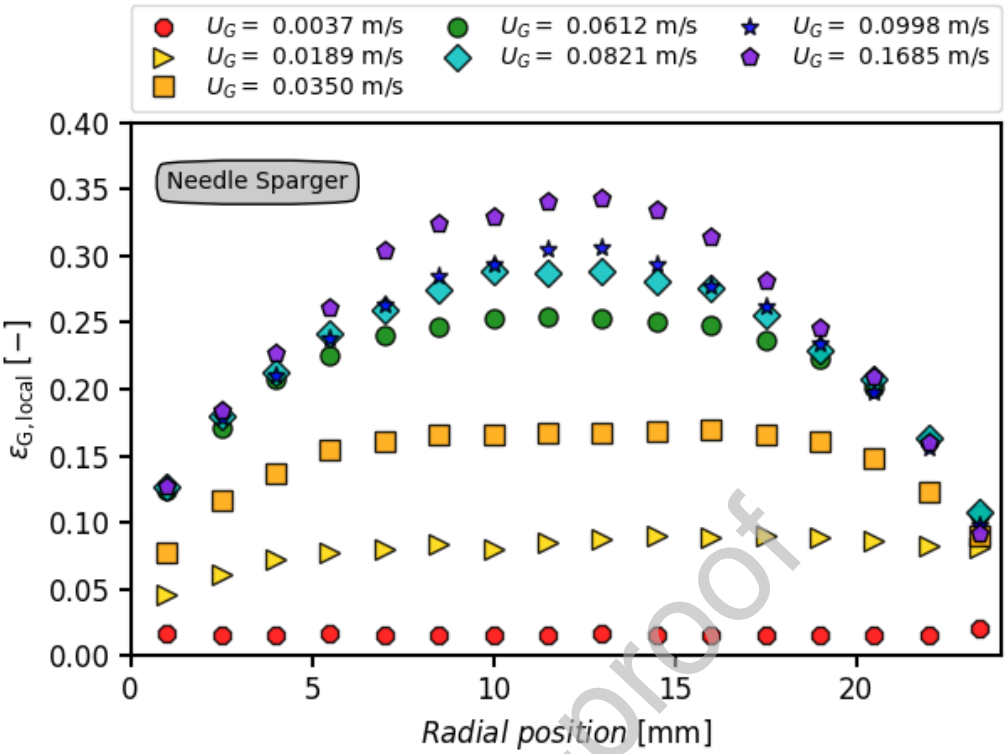


(a) local gas holdup

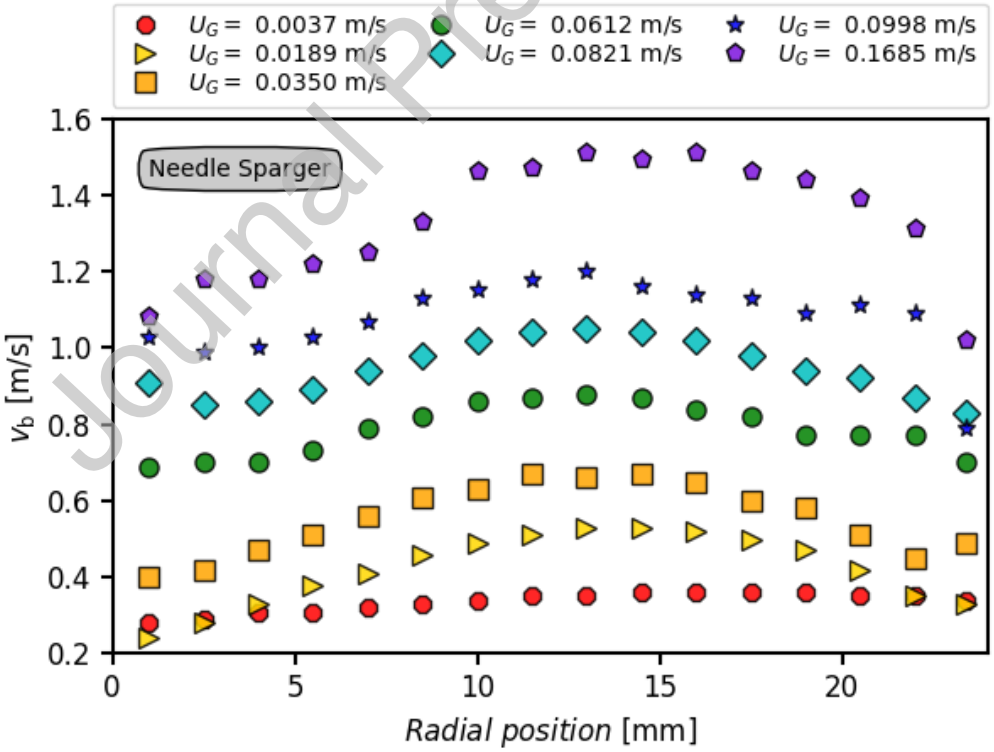


(b) local gas velocity

**Figure 15.** *Optical probe measurements for the needle gas sparger – batch mode.*

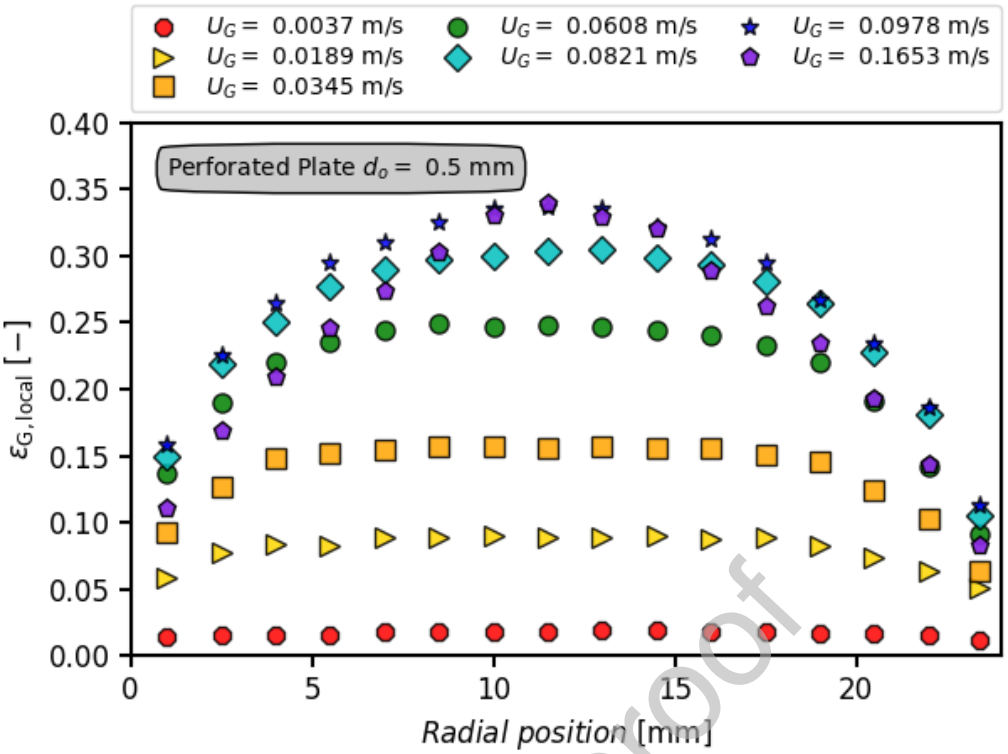


(a) local gas holdup

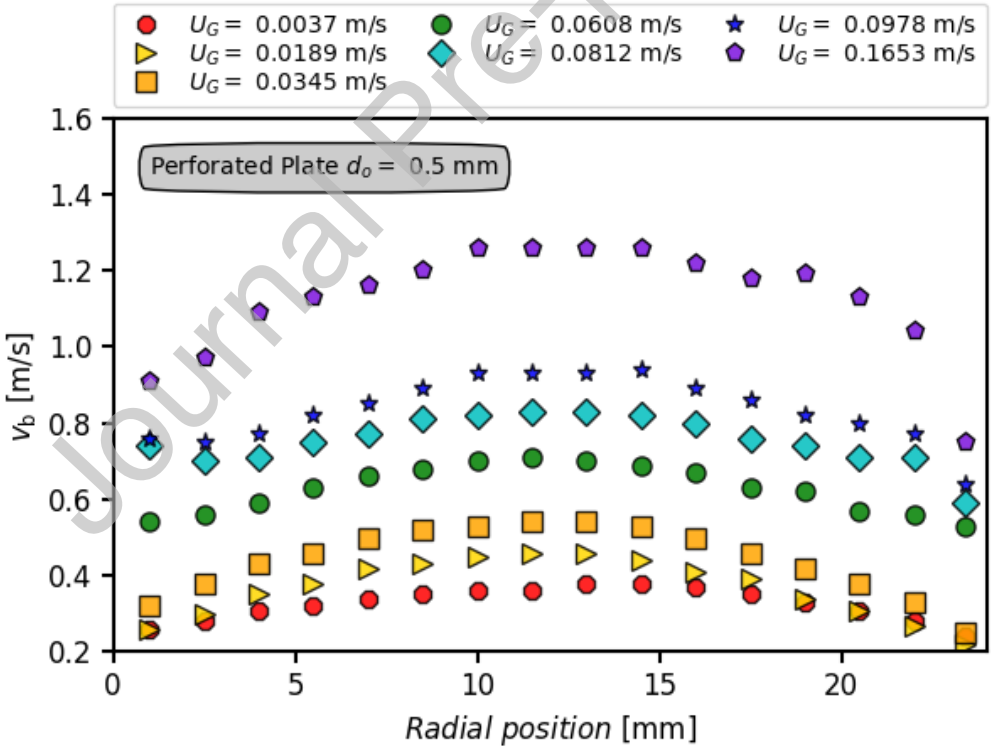


(b) local gas velocity

**Figure 16.** *Optical probe measurements for the perforated plate ($d_0$ = 0.5 mm) gas sparger.*

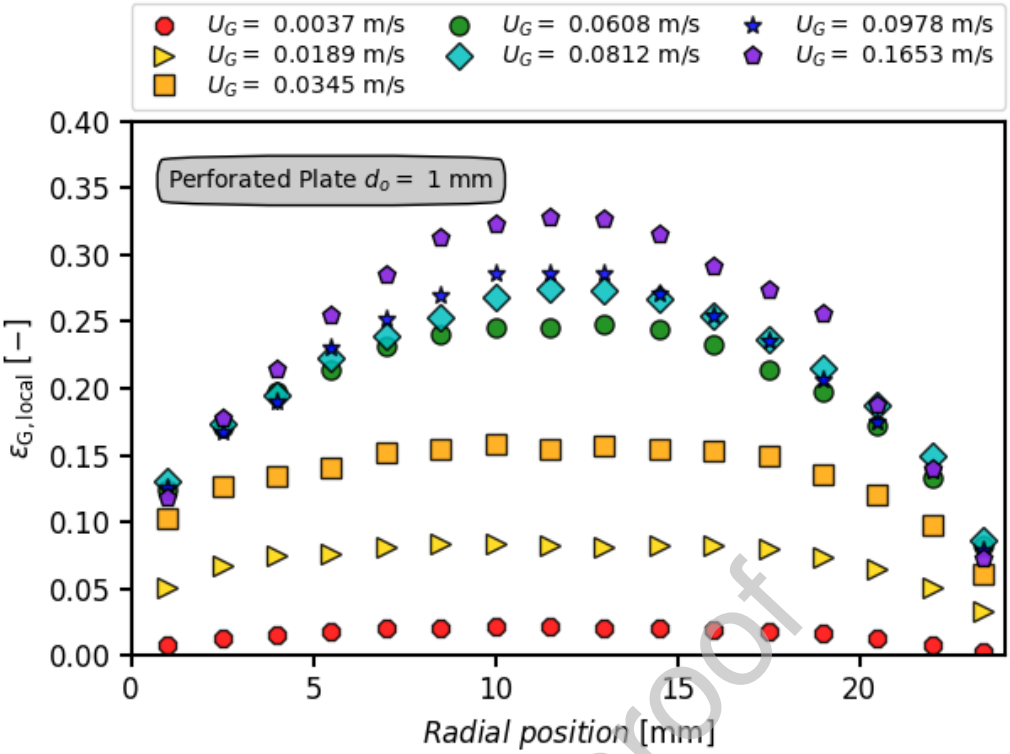


(a) local gas holdup

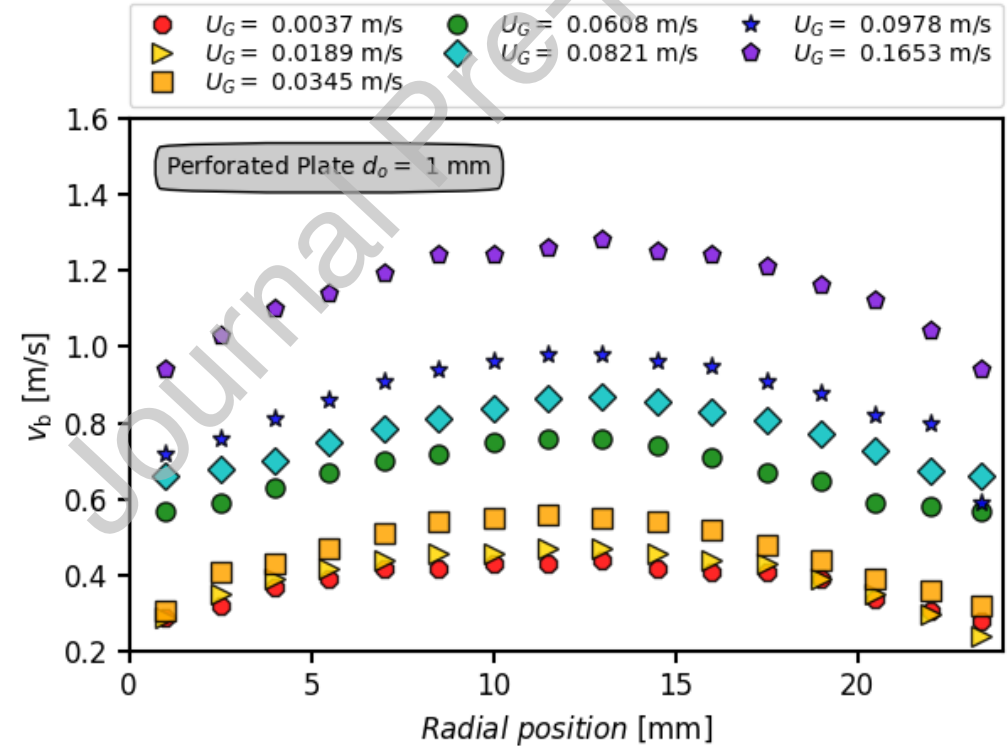


(b) local gas velocity

**Figure 17.** *Optical probe measurements for the perforated plate ($d_0$ = 1.0 mm) gas sparger.*

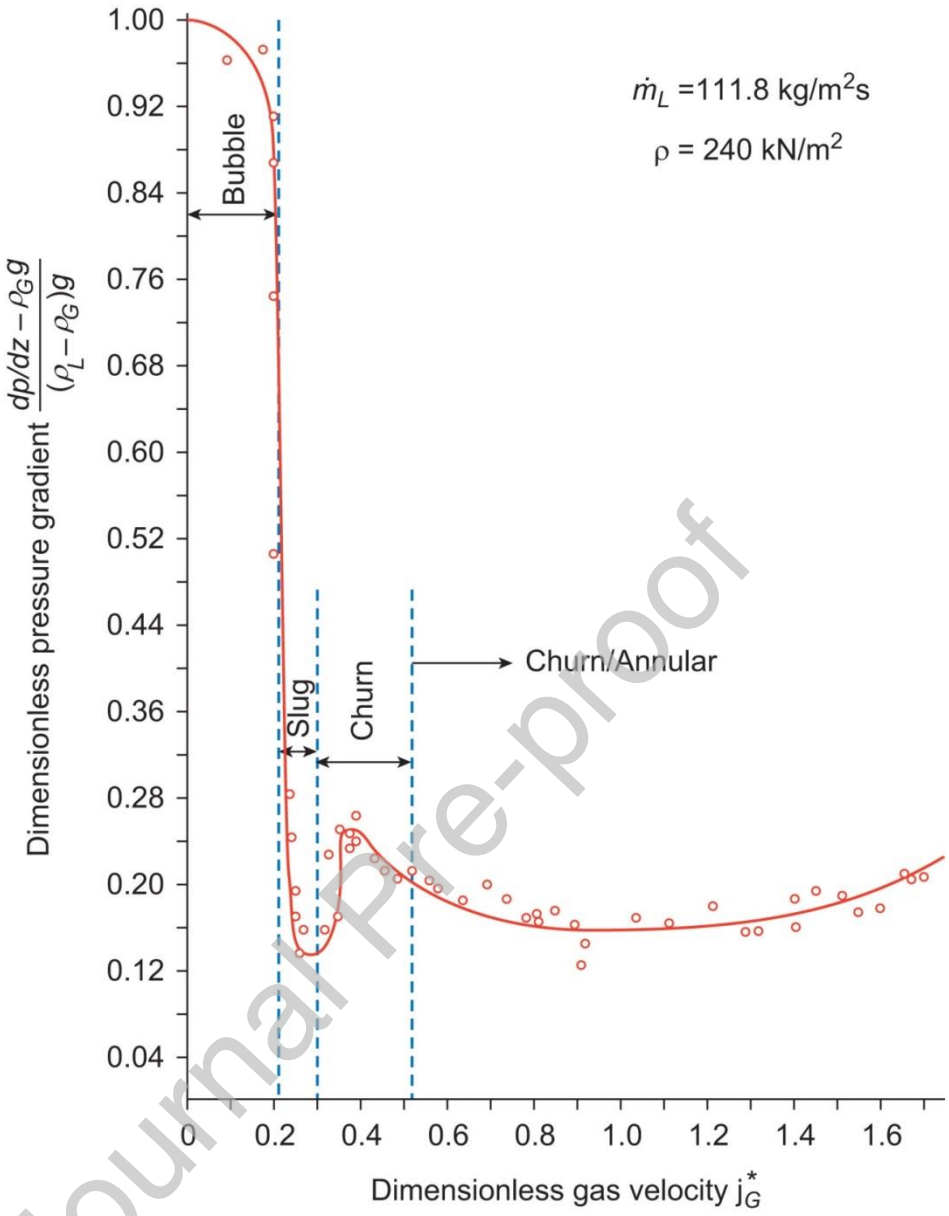




**Figure 18.** *Pressure gradient distribution against dimensionless gas velocity for gas–liquid flow in vertical pipes proposed by (Owen, 1986) – from ref. (Montoya et al., 2016).*

**Table 1.** *Literature studies used for comparison purposes.*

| Ref. | Figure | $d_c$ [m] | $H_c$ [m] | $H_0$ [m] | AR [-] | Sparger Type | $d_o$ [mm] |
|---|---|---|---|---|---|---|---|
| (Sasaki et al., 2017) | Figure 6a and 6b | 0.16, circular | - | 0.4 up to 1.8 | 2.25 – 6.25 | Perforated plate | 1.4 |
| | | 0.20, circular | - | 0.4 up to 1.8 | 2 – 5 | Perforated plate | 1.4 |
| | | 0.30, circular | - | 0.4 up to 1.8 | 2 – 3.33 | Perforated plate | 1.4 |
| | | 0.45, circular[#] | 7 | - | - | Plate-type | 5 |
| | | 2.00, circular | 7 | 3 up to 4 | 1.5 – 2 | Arm-type | 5 |
| (Sasaki et al., 2016) | Figure 6c | 0.2, circular and square | 2 | 0.3 up to 1 | 1.5 up to 5 | Perforated plate | 1.4 |
| (Rollbush et al, 2015) | Figure 6d | 0.16, circular | 1.8 | 1.8 | 11.25 | Perforated Plate | 1 |
| | | 0.30, circular | 2.63 | 2.63 | 8.75 | | |
| | | 0.33, circular and under pressure up to 3.6 MPa | 3.88 | 3.88 | 11.25 | | |
| (Ruzicka et al., 2001a) | Figure 5a | 0.14/0.29/0.4, circular | | 0.1 up to 1.2 | 0.25 up to 8.5 | Perforated plate | 0.5 |
| (Thorat et al., 1998) | Figure 5b | 0.385, circular | 3.2 | 0.385 up to 2.695 | 1 up to 7 | Perforated plate | 1 |
| (Zahradnik et al., 1997) | Figure 5a | 0.14/0.15/0.29, cicular | 2.6 | 0.25 up to 10 | 1 up to 29 | Perforated plate | 0.5/1.6 |
| (Wilkinson et al., 1992) | Figure 5d | 0.158/0.23, circular | - | 1.5/1.2 | 5 up to 10 | Ring | 2 up to 7 |
| (Reilly et al, 1986) | Figure 5d | 0.30, circular | 5.0 | 3 | 10* | Single orifice | 25.4 |
| (Schumpe and Grund, 1986) | Figure 5d | 0.30, circular | 4.4 | - | 10* | Ring plate *(perforated plate sparger is not considered here)* | 1 |
| (Patil et al, 1984) | Figure 5c | 0.38, sectionalized bubble column | | 0.684/1.026/1,406 | 1.8/2.7 and 3.7 | Perforated plate *(single point sparger is not considered here)* | 3.57 |
| (Akita, 1973) | Figure 5d | 0.152, circular | 4 | 2 up to 3 | 13.2 up to 19.7 | single-hole nozzle | 5 |
| (Yoshida and Akita, 1965) | Figure 5d | 0.077/0.152/0.301/0.6, circular | - | 0.9 up to 3.5 | 2.1 up to 22.9 | Single-hole nozzle | 2.25 up to 40 |

[#] *In this case, the relationship between the superficial gas velocity and the gas holdup (the gas holdup curve) was not presented and it is not considered in this study.*

*Estimated from the gas holdup data

**Table 2.** *Flow regime transition points for the needle gas sparger.*

| AR [-] | Presence of the mono-dispersed homogeneous flow regime | Flow regime transition $t_1$ | | Presence of the poly-dispersed homogeneous flow regime (pre-transition flow regime) | Flow regime transition $t_2$ | | Presence of the transition flow regime (no coalescence-induced structures) | Flow regime transition $t_3$ | | Presence of the transition flow regime (coalescence-induced structures) | Flow regime transition $t_4$ | | Presence of the pseudo-heterogeneous flow regime | Flow regime transition $t_5$ | | Presence of the pure-heterogeneous flow regime |
|---|---|---|---|---|---|---|---|---|---|---|---|---|---|---|---|---|
| | | $\varepsilon_G$ [-] | $U_G$ [m/s] | | $\varepsilon_G$ [-] | $U_G$ [m/s] | | $\varepsilon_G$ [-] | $U_G$ [m/s] | | $\varepsilon_G$ [-] | $U_G$ [m/s] | | $\varepsilon_G$ [-] | $U_G$ [m/s] | |
| 1 | yes | 0.2522 | 0.0398 | yes | 0.5951 | 0.0937 | yes | 0.6207 | 0.1143 | yes | 0.5720 | 0.2288 | yes | - | - | not detected (out of the range of UG) |
| 2 | yes | 0.2331 | 0.0397 | yes | 0.4712 | 0.0929 | yes | 0.5245 | 0.1488 | yes | 0.5164 | 0.1954 | yes | - | - | not detected (out of the range of UG) |
| 5 | yes | 0.2036 | 0.0359 | yes | 0.3264 | 0.1006 | no | - | - | no | - | - | no | - | - | yes |
| 7.5 | yes | 0.1909 | 0.0395 | yes | 0.2582 | 0.0679 | no | - | - | no | - | - | no | - | - | yes |
| 10 | yes | 0.1757 | 0.0324 | yes | 0.2425 | 0.0622 | no | - | - | no | - | - | no | - | - | yes |
| 12.5 | yes | 0.1809 | 0.0350 | yes | 0.2436 | 0.0666 | no | - | - | no | - | - | yes | 0.2493 | 0.0998 | yes |
| 15 | yes | 0.1830 | 0.0389 | yes | 0.2383 | 0.0625 | no | - | - | no | - | - | yes | 0.2252 | 0.0839 | yes |

**Table 3.** *Flow regime transition points for the perforated plate ($d_0$ = 0.5 mm) gas sparger.*

| AR [-] | Presence of the mono-dispersed homogeneous flow regime | Flow regime transition $t_1$ | | Presence of the poly-dispersed homogeneous flow regime (pre-transition flow | Flow regime transition $t_2$ | | Presence of the transition flow regime (no coalescence-induced structures) | Flow regime transition $t_3$ | | Presence of the transition flow regime (coalescence-induced structures) | Flow regime transition $t_4$ | | Presence of the pseudo-heterogeneous flow regime | Flow regime transition $t_5$ | | Pure-heterogeneous |
|---|---|---|---|---|---|---|---|---|---|---|---|---|---|---|---|---|
| | | $\varepsilon_G$ [-] | $U_G$ [m/s] | | $\varepsilon_G$ [-] | $U_G$ [m/s] | | $\varepsilon_G$ [-] | $U_G$ [m/s] | | $\varepsilon_G$ [-] | $U_G$ [m/s] | | $\varepsilon_G$ [-] | $U_G$ [m/s] | |

| | | | | regime) | | | | | | | | | | | |
|---|---|---|---|---|---|---|---|---|---|---|---|---|---|---|---|
| 1 | yes | 0.2636 | 0.0403 | yes | 0.5208 | 0.0898 | yes | 0.5470 | 0.1046 | yes | 0.4351 | 0.2336 | yes | - | - | not detected (out of the range of UG) |
| 2 | yes | 0.2143 | 0.0395 | yes | 0.4229 | 0.0854 | yes | 0.4417 | 0.0982 | yes | 0.3883 | 0.1923 | yes | 0.3804 | 0.1612 | yes |
| 5 | yes | 0.2004 | 0.0394 | yes | 0.2989 | 0.0727 | yes | 0.3313 | 0.0838 | yes | 0.2826 | 0.1161 | yes | 0.3017 | 0.2188 | yes |
| 7.5 | yes | 0.1920 | 0.0391 | yes | 0.2870 | 0.0721 | yes | 0.3083 | 0.0828 | yes | 0.2539 | 0.1172 | yes | 0.2651 | 0.1719 | yes |
| 10 | yes | 0.1598 | 0.0348 | yes | 0.2721 | 0.0711 | yes | 0.2939 | 0.0816 | yes | 0.2463 | 0.1123 | yes | 0.2648 | 0.1696 | yes |
| 12.5 | yes | 0.1777 | 0.0386 | yes | 0.2795 | 0.0754 | yes | 0.2914 | 0.0812 | yes | 0.2241 | 0.1181 | yes | 0.2365 | 0.1742 | yes |
| 15 | yes | 0.1742 | 0.0385 | yes | 0.2621 | 0.0702 | yes | 0.2827 | 0.0856 | yes | 0.2273 | 0.1160 | yes | 0.2339 | 0.1540 | yes |

**Table 4.** *Flow regime transition points for the perforated plate ($d_0$ = 1.0 mm) gas sparger.*

| AR [-] | Presence of the mono-dispersed homogeneous flow regime | Flow regime transition $t_1$ | | Presence of the poly-dispersed homogeneous flow regime (pre-transition flow regime) | Flow regime transition $t_2$ | | Presence of the transition flow regime (no coalescence-induced structures) | Flow regime transition $t_3$ | | Presence of the transition flow regime (coalescence-induced structures) | Flow regime transition $t_4$ | | Presence of the pseudo-heterogeneous flow regime | Flow regime transition $t_5$ | | Presence of the pure-heterogeneous flow regime |
|---|---|---|---|---|---|---|---|---|---|---|---|---|---|---|---|---|
| | | $\varepsilon_G$ [-] | $U_G$ [m/s] | | $\varepsilon_G$ [-] | $U_G$ [m/s] | | $\varepsilon_G$ [-] | $U_G$ [m/s] | | $\varepsilon_G$ [-] | $U_G$ [m/s] | | $\varepsilon_G$ [-] | $U_G$ [m/s] | |
| 1 | yes | 0.2206 | 0.0309 | yes | 0.4902 | 0.0915 | yes | 0.5383 | 0.1119 | yes | 0.3844 | 0.2336 | yes | - | - | not detected (out of the range of UG) |
| 2 | yes | 0.1636 | 0.0398 | yes | 0.3512 | 0.0872 | yes | 0.3820 | 0.0984 | yes | 0.3590 | 0.1488 | yes | 0.3555 | 0.1910 | yes |
| 5 | yes | 0.1458 | 0.0393 | yes | 0.2568 | 0.0833 | yes | 0.2808 | 0.1152 | yes | 0.2690 | 0.1319 | yes | 0.2769 | 0.1559 | yes |
| 7.5 | yes | 0.1448 | 0.0348 | yes | 0.2339 | 0.0670 | yes | 0.2416 | 0.0771 | yes | 0.2410 | 0.0880 | yes | 0.2439 | 0.1001 | yes |
| 10 | yes | 0.1449 | 0.0327 | yes | 0.2257 | 0.0614 | yes | 0.2427 | 0.0713 | yes | 0.2331 | 0.0872 | yes | 0.2463 | 0.1250 | yes |
| 12.5 | yes | 0.1452 | 0.0325 | yes | 0.2166 | 0.0608 | yes | 0.2267 | 0.0812 | yes | 0.2331 | 0.0978 | yes | 0.2306 | 0.1329 | yes |
| 15 | yes | 0.1454 | 0.0343 | yes | 0.2223 | 0.0748 | no | - | - | no | - | - | yes | 0.2215 | 0.1028 | yes |

**Table 5.** *Flow regime transition points for the spider gas sparger.*

| AR [-] | Presence of the mono-dispersed homogeneous flow regime | Flow regime transition $t_1$ | | Presence of the poly-dispersed homogeneous flow regime (pre-transition flow regime) | Flow regime transition $t_2$ | | Presence of the transition flow regime (no coalescence-induced structures) | Flow regime transition $t_3$ | | Presence of the transition flow regime (coalescence-induced structures) | Flow regime transition $t_4$ | | Presence of the pseudo-heterogeneous flow regime | Flow regime transition $t_5$ | | Presence of the pure-heteregeneous flow regime |
|---|---|---|---|---|---|---|---|---|---|---|---|---|---|---|---|---|
| | | $\varepsilon_G$ [-] | $U_G$ [m/s ] | | $\varepsilon_G$ [-] | $U_G$ [m/s ] | | $\varepsilon_G$ [-] | $U_G$ [m/s ] | | $\varepsilon_G$ [-] | $U_G$ [m/s ] | | $\varepsilon_G$ [-] | $U_G$ [m/s ] | |
| 1 | no | - | - | yes | 0.1208 | 0.0349 | no | - | - | no | - | - | no | - | - | yes |
| 2 | no | - | - | yes | 0.1151 | 0.0315 | no | - | - | no | - | - | no | - | - | yes |
| 5 | no | - | - | yes | 0.0000 | 0.0000 | no | - | - | no | - | - | no | - | - | yes |
| 7.5 | no | - | - | yes | 0.0932 | 0.0291 | no | - | - | no | - | - | no | - | - | yes |
| 10 | no | - | - | yes | 0.0963 | 0.0291 | no | - | - | no | - | - | no | - | - | yes |
| 12.5 | no | - | - | yes | 0.0973 | 0.0290 | no | - | - | no | - | - | no | - | - | yes |
| 15 | no | - | - | yes | 0.0988 | 0.0267 | no | - | - | no | - | - | no | - | - | yes |

**Table 6.** *Flow regime transition points for the spider gas sparger operated in counter-current mode ($U_L$ = -0.0846 m/s): influence of the aspect ratio.*

| AR [-] | Presence of the mono-dispersed homogeneous flow regime | Flow regime transition $t_1$ | | Presence of the poly-dispersed homogeneous flow regime (pre-transition flow regime) | Flow regime transition $t_2$ | | Presence of the transition flow regime (no coalescence-induced structures) | Flow regime transition $t_3$ | | Presence of the transition flow regime (coalescence-induced structures) | Flow regime transition $t_4$ | | Presence of the pseudo-heterogeneous flow regime | Flow regime transition $t_5$ | | Presence of the pure-heteregeneous flow regime |
|---|---|---|---|---|---|---|---|---|---|---|---|---|---|---|---|---|
| | | $\varepsilon_G$ [-] | $U_G$ [m/s ] | | $\varepsilon_G$ [-] | $U_G$ [m/s ] | | $\varepsilon_G$ [-] | $U_G$ [m/s ] | | $\varepsilon_G$ [-] | $U_G$ [m/s ] | | $\varepsilon_G$ [-] | $U_G$ [m/s ] | |
| 5 | no | - | - | yes | 0,1519 | 0,0292 | no | - | - | no | - | - | no | - | | yes |
| 7,5 | no | - | - | yes | 0,1481 | 0,0331 | no | - | - | no | - | - | no | - | | yes |
| 10 | no | - | - | yes | 0,1257 | 0,0248 | no | - | - | no | - | - | no | - | | yes |
| 12,5 | no | - | - | yes | 0,1071 | 0,0188 | no | - | - | no | - | - | no | - | | yes |
| 15 | no | - | - | yes | 0,1067 | 0,0186 | no | - | - | no | - | - | no | - | | yes |

**Table 7.** *Flow regime transition points for the spider gas sparger operated in counter-current mode: influence of the liquid velocity.*

| $U_L$ [m/s ] | Presence of the mono-dispersed homogeneous flow regime | Flow regime transition $t_1$ | | Presence of the poly-dispersed homogeneous flow regime (pre-transition flow regime) | Flow regime transition $t_2$ | | Presence of the transition flow regime (no coalescence-induced structures) | Flow regime transition $t_3$ | | Presence of the transition flow regime (coalescence-induced structures) | Flow regime transition $t_4$ | | Presence of the pseudo-heterogeneous flow regime | Flow regime transition $t_5$ | | Presence of the pure-heteregeneous flow regime |
|---|---|---|---|---|---|---|---|---|---|---|---|---|---|---|---|---|
| | | $\varepsilon_G$ [-] | $U_G$ [m/s ] | | $\varepsilon_G$ [-] | $U_G$ [m/s ] | | $\varepsilon_G$ [-] | $U_G$ [m/s ] | | $\varepsilon_G$ [-] | $U_G$ [m/s ] | | $\varepsilon_G$ [-] | $U_G$ [m/s ] | |
| 0 | no | - | - | yes | 0,0901 | 0,0266 | no | - | - | no | - | - | no | - | - | yes |
| -0,017 | no | - | - | yes | 0,0988 | 0,0266 | no | - | - | no | - | - | no | - | - | yes |
| -0,033 | no | - | - | yes | 0,1066 | 0,0286 | no | - | - | no | - | - | no | - | - | yes |
| -0,051 | no | - | - | yes | 0,1098 | 0,0228 | no | - | - | no | - | - | no | - | - | yes |
| -0,066 | no | - | - | yes | 0,1137 | 0,0208 | no | - | - | no | - | - | no | - | - | yes |
| -0,092 | no | - | - | yes | 0,1176 | 0,0188 | no | - | - | no | - | - | yes | 0,1537 | 0,1537 | yes |

**Table 8.** *Flow regime transition points for the pipe sparger (open tube configuration) operated in counter-current mode: influence of the liquid velocity.*

| $U_L$ [m/s ] | Presence of the mono-dispersed homogeneous flow regime | Flow regime transition $t_1$ | | Presence of the poly-dispersed homogeneous flow regime (pre-transition flow regime) | Flow regime transition $t_2$ | | Presence of the transition flow regime (no coalescence-induced structures) | Flow regime transition $t_3$ | | Presence of the transition flow regime (coalescence-induced structures) | Flow regime transition $t_4$ | | Presence of the pseudo-heterogeneous flow regime | Flow regime transition $t_5$ | | Presence of the pure-heteregeneous flow regime |
|---|---|---|---|---|---|---|---|---|---|---|---|---|---|---|---|---|
| | | $\varepsilon_G$ [-] | $U_G$ [m/s ] | | $\varepsilon_G$ [-] | $U_G$ [m/s ] | | $\varepsilon_G$ [-] | $U_G$ [m/s ] | | $\varepsilon_G$ [-] | $U_G$ [m/s ] | | $\varepsilon_G$ [-] | $U_G$ [m/s ] | |
| 0 | no | - | - | yes | 0,0634 | 0,0167 | no | - | - | no | - | - | no | - | - | 0 |
| -0,033 | no | - | - | yes | 0,0695 | 0,0167 | no | - | - | no | - | - | no | - | - | -0,033 |
| -0,04 | no | - | - | yes | 0,0759 | 0,0167 | no | - | - | no | - | - | no | - | - | -0,04 |
| -0,066 | no | - | - | yes | 0,0779 | 0,0148 | no | - | - | no | - | - | no | - | - | -0,066 |
| -0,08 | no | - | - | yes | 0,0733 | 0,0129 | no | - | - | no | - | - | no | - | - | -0,08 |
| -0,092 | no | - | - | yes | 0,0808 | 0,0129 | no | - | - | no | - | - | yes | 0,1561 | 0,1561 | -0,092 |

**Table 9.** *Flow regime transition points for the pipe sparger (annular gap configuration) operated in counter-current mode: influence of the liquid velocity.*

| $U_L$ [m/s ] | Presence of the mono-dispersed homogeneous flow regime | Flow regime transition $t_1$ | | Presence of the poly-dispersed homogeneous flow regime (pre-transition flow regime) | Flow regime transition $t_2$ | | Presence of the transition flow regime (no coalescence-induced structures) | Flow regime transition $t_3$ | | Presence of the transition flow regime (coalescence-induced structures) | Flow regime transition $t_4$ | | Presence of the pseudo-heterogeneous flow regime | Flow regime transition $t_5$ | | Presence of the pure-heteregeneous flow regime |
|---|---|---|---|---|---|---|---|---|---|---|---|---|---|---|---|---|
| | | $\varepsilon_G$ [-] | $U_G$ [m/s ] | | $\varepsilon_G$ [-] | $U_G$ [m/s ] | | $\varepsilon_G$ [-] | $U_G$ [m/s ] | | $\varepsilon_G$ [-] | $U_G$ [m/s ] | | $\varepsilon_G$ [-] | $U_G$ [m/s ] | |
| 0 | no | - | - | yes | 0,0888 | 0,0266 | no | - | - | no | - | - | no | - | - | 0 |
| -0,039 | no | - | - | yes | 0,0914 | 0,0220 | no | - | - | no | - | - | no | - | - | -0,039 |
| -0,079 | no | - | - | yes | 0,0981 | 0,0198 | no | - | - | no | - | - | no | - | - | -0,079 |
| -0,109 | no | - | - | yes | 0,1127 | 0,0175 | no | - | - | no | - | - | no | - | - | -0,109 |